Asymmetric division coordinates collective cell migration in angiogenesis

Guilherme Costa[1,4], Kyle I. Harrington[2, 4], Holly E. Lovegrove[1,4], Donna J. Page[1], Shilpa Chakravartula[2], Katie Bentley[2], Shane P. Herbert[1,3]

[1]Faculty of Biology, Medicine and Health, Michael Smith Building, University of Manchester, Oxford Road, Manchester, M13 9PT, UK. [2]Computational Biology Laboratory, Center for Vascular Biology Research, Beth Israel Deaconess Medical Center, Harvard Medical School, Boston, Massachusetts 02215, USA.

[4] These authors contributed equally to this work

[3] Correspondence should be addressed to S.P.H. (e-mail: shane.herbert@manchester.ac.uk)

The asymmetric division of stem or progenitor cells generates daughters with distinct fates and regulates cell diversity during tissue morphogenesis. However, roles for asymmetric division in other more dynamic morphogenetic processes, such as cell migration, have not previously been described. Here we combine zebrafish *in vivo* experimental and computational approaches to reveal that heterogeneity introduced by asymmetric division generates multicellular polarity that drives coordinated collective cell migration in angiogenesis. We find that asymmetric positioning of the mitotic spindle during endothelial tip cell division generates daughters of distinct size with discrete "tip" or "stalk" thresholds of pro-migratory Vegfr signalling. Consequently, post-mitotic Vegfr asymmetry drives Dll4/Notch-independent self-organisation of daughters into leading tip or trailing stalk cells, and disruption of asymmetry randomises daughter tip/stalk selection. Thus, asymmetric division seamlessly integrates cell proliferation with collective migration, and as such, may facilitate growth of other collectively migrating tissues during development, regeneration and cancer invasion.

Organogenesis requires the precise integration of diverse morphogenetic processes. For example, in angiogenesis the coordinated specification, proliferation and collective migration of leading "tip" and trailing "stalk" endothelial cells drives nascent blood vessel formation[1-3]. Activation of VEGFR-2/-3 signalling by gradients of VEGF ligand induces tip cell (TC) formation and directed migration[3,4]. Moreover, VEGFR activation promotes expression of the Notch ligand delta-like 4 (Dll4) in TCs, which activates Notch in adjacent stalk cells (SCs) to down-regulate VEGFR function and laterally inhibit TC identity[5-8]. Consequently, relative levels of *Vegfr* and/or *Dll4* expression directly influence TC selection and collective migration via VEGFR-Notch feedback[9,10].

Cell proliferation is also essential for new vessel growth[11,12], but it is unclear how cell divisions, which must inherently partition VEGFR and Notch signalling components between daughters, do not disrupt hierarchical tip-stalk organisation and synchronised collective movements. For example, symmetrical partitioning of VEGFR-2 and Dll4 during TC division would prompt competition between daughters for re-assignment of TC identity. Considering that the temporal dynamics of Delta-Notch-mediated lateral inhibition are relatively slow (upwards of 5h)[13,14], division would severely impede angiogenesis (Supplementary Fig. 1a). Hence, it is unknown how multicellular polarity and uninterrupted directed collective migration are maintained during proliferative growth.

RESULTS

Endothelial cell divisions generate asymmetric daughters

To investigate the post-mitotic dynamics of tip-stalk re-selection we performed a detailed analysis of tip/stalk behaviour at single cell resolution *in vivo*. Live-cell

imaging of intersegmental vessel (ISV) sprouting in *Tg(kdrl:nlsEGFP)*^{zf109} zebrafish embryos indicated that endothelial cell movements were highly characteristic and dependent on cell positioning within new branches (Fig. 1a to e; Supplementary Fig. 1b, c). Tracking of individual nuclei revealed that ISV TCs move dorsally from the dorsal aorta (DA) to the dorsolateral anastomotic vessel (DLAV) position at quicker rates than adjacent SCs (Supplementary Fig. 1b, c; Supplementary Video 1). Further analyses of single lyn-mCherry-expressing cells revealed that TCs rapidly migrated (Fig. 1a, c; Supplementary Video 2) whereas SCs were less motile and alternatively underwent cell elongation[15] (Fig. 1b, d; Supplementary Video 3). Moreover, averaging of multiple datasets indicated that cells exhibit wide variance in motility (Supplementary Fig. 1d) but revealed that the first, second and third endothelial cells to sprout from the DA (the leading TC, adjacent SC and following SC, respectively) displayed highly characteristic motilities during ISV branching (Fig. 1e). During ISV sprouting, 76% of TCs and 27% of SCs divided (Supplementary Fig. 1e), with mitosis oriented perpendicular to the vessel long axis, as previously described[16,17]. However, continued tracking of the distal-most daughter of TC or SC divisions demonstrated that mitosis had no effect on movement, relative to non-dividing cells (Fig. 1f). Hence, characteristic behaviour was instantly re-established following division without pausing for tip/stalk re-selection. Consistent with these observations, tracking of daughter cells after completion of mitosis (Supplementary Fig. 1f) revealed that the tip-stalk hierarchy and characteristic TC/SC motilities were seamlessly re-established following division (Fig. 1g to l; Supplementary Fig. 1g, h). For example, distal TC daughters (cell 1.1) retained TC-like movement whereas proximal daughters (cell 1.2) instantly adopted the motility of SCs (Fig. 1g, i to l; Supplementary Video 4). Similarly, only distal daughters of SC divisions

retained parental motility (Fig. 1h, i and Supplementary Video 5). Hence, daughters rapidly self-organise into leading and trailing cells following division, which maintains uninterrupted collective migration during vessel proliferation (Fig. 2g).

Post-mitotic tip/stalk selection is Dll4/Notch-independent

To confirm that this represents a Dll4/Notch-independent mechanism, *dll4* expression was abrogated using a well-validated morpholino oligonucleotide[5]. In the absence of *dll4*, lateral inhibition of TC identity was lost and non-dividing cells at SC positions atypically exhibited TC-like motilities (Fig. 2a-c and Supplementary Video 6). Despite this, daughters of TC and SC divisions still displayed differential motilities, with only the distal daughter retaining parental behaviour (Fig. 2d to f and Supplementary Videos 7 and 8). Similar results were obtained upon inhibition of Notch signalling using the γ-secretase inhibitor, dibenzazepine (DBZ; Supplementary Fig. 2a, b). Hence, endothelial cell division generates daughters with differential motilities, independent of Dll4/Notch-mediated lateral inhibition. Although Dll4-Notch signalling did not determine post-mitotic behaviour, it likely reinforce differences introduced by division, as proximal daughters of *dll4*-deficient TC divisions recovered to be more motile than controls 5h after division (cell 1.2; Fig. 2f). Interestingly, slower proximal daughters of TC divisions were frequently overtaken by adjacent SCs (Fig. 2d). Likewise, the distal daughters of SC divisions were faster than and often overtook the slower proximal daughters of TC divisions (Supplementary Fig. 2c, d). Hence proximo-distal positioning within the ISV, the cell-cell junctional context and/or proximity of cells to Vegf ligand after division do not account for observed differences in daughter motility (Fig. 2g, h).

Overall, these findings reveal a Dll4/Notch-independent role for mitosis in tip/stalk selection and suggest that endothelial cell divisions may be intrinsically asymmetric.

in silico prediction of asymmetric cell division

Asymmetric division determines differential daughter cell fate in many systems[18,19], but has not been implicated in the control of cell motility. To investigate a potential role for asymmetric division in collective migration we adapted our previously validated MemAgent-Spring computational Model (MSM) of Notch/Vegf-mediated tip/stalk selection[20,21] to accurately replicate *in vivo* TC and SC dynamics observed during ISV branching (Supplementary Fig. 3). Importantly, the MSM was extended/adapted to facilitate a simple cell division function and improved lamella extension/retraction functionality (Supplementary Fig. 4a, b; see Methods). The key assumptions that determine the behavior of the MSM can be summarised as (1) ISVs branch in response to a Vegf gradient; (2) binding of Vegf to Vegfr induces the formation of filopodia and lamellipodia; (3) the amount of filopodia and lamellipodia determines the rate of cell migration; (4) upon cell division Vegfr mRNA and protein are partitioned between daughter cells according to their present localisations; (5) a slower-acting Dll4-Notch-Vegfr-mediated mechanism then determines daughter TC and SC phenotypes. Once calibrated to match *in vivo* TC and SC dynamics in the absence of cell division (Supplementary Fig. 3b, c), further simulation of symmetric division was not sufficient to replicate biological data (Fig. 3a; Supplementary Video 9). Simulations of symmetric divisions that equally partitioned Vegfr mRNA and protein between daughter cells resulted in daughters that were less motile than the parental TC. These symmetric daughters then actively competed for the tip position and mutually repressed each

other's motility via time-consuming Dll4-Notch oscillations, slowing down ISV branching (Fig. 3a). In contrast, simulation of asymmetric divisions to create daughters that differentially partitioned key components of the MSM (cell size, Vegfr protein, *vegfr* mRNA; see methods) generated daughters with distinct tip and stalk cell-like behaviours (Fig. 3b; Supplementary Video 10). The MSM indicated that asymmetric divisions rapidly generated daughters with distinct motilities by ensuring that one daughter retained higher levels of Vegfr signalling (Fig. 3b). The model therefore predicted that asymmetric division rather than symmetric division of these key components is necessary to generate the observed post mitotic motilities.

Asymmetric division generates daughters of distinct size.

To validate this *in silico* prediction *in vivo* we first quantified post-mitotic differences in cell size, a key hallmark of asymmetric division[18,19]. Firstly, nuclear localised Eos fluorescent protein expressed in TCs of *Tg(kdrl:nlsEos)*^{ncv6} embryos was irreversibly and stably photoconverted from green (gEos) to red (rEos) using 405nm light (Fig. 3c, d). The nuclear localisation signal fused to Eos ensured dispersal of the stable pool of rEos throughout the cytoplasm upon mitotic nuclear envelope breakdown (Supplementary Fig. 5a), followed by partitioning between daughters at cytokinesis and re-distribution to daughter cell nuclei after reassembly of the nuclear envelope (Fig. 3c, e). Importantly, the sum total of nuclear rEos subsequently inherited by both daughter cells exactly corresponded to the initial levels found in parental tip cells (Fig. 3f). Hence, post-mitotic nuclear rEos levels were a direct readout of the relative partitioning of cytoplasmic volumes of TC daughters at cytokinesis. Consistent with *in silico* predictions, differential inheritance of photoconverted rEos confirmed that TC divisions

were intrinsically asymmetric and generated daughters of distinct size (Fig. 3e, f). Moreover, similar analysis of sprouting mesencephalic veins revealed that asymmetric division was a conserved feature of migrating TCs (Supplementary Fig. 5b-e). Asymmetries in TC daughter size were further confirmed upon analysis of single dividing TCs, with distal daughters of TC divisions being consistently 1.8 to 1.9 times larger than proximal daughters (Fig. 4a, b). Importantly, larger TC daughters were consistently more motile than smaller cells (Fig. 4c) and the size of individual TC daughters was directly correlated with their rate of post-mitotic motility (Fig. 4d). Lastly, the difference between the sizes of both daughters from TC divisions (distal cell size – proximal cell size) was putatively correlated with resulting differences in daughter cell motility (distal cell motility – proximal cell motility), but critically, in rare cases where daughters were near symmetrically sized they displayed near identical motilities (Fig. 4e). Hence, intrinsically asymmetric divisions coordinate collective cell migration *in vivo* by generating TC daughters of differential size and motility.

Polarised positioning of the mitotic spindle drives asymmetric division

Asymmetric positioning of the mitotic spindle is known to drive asymmetric division of stem/progenitor cells in many systems[18,19]. As such, to define the mechanistic basis of post-mitotic asymmetries in tip cell daughter size, we investigated spindle positioning during tip cell division. High temporal resolution *in vivo* live imaging of tip cells expressing α-tubulin-GFP revealed that, after initially assuming a central position, the entire mitotic spindle consistently shifted to the proximal pole of dividing tip cells during metaphase (Fig. 4f; Supplementary Video 11). Consequently, the plane of tip cell division was proximally biased during anaphase and telophase, generating

daughters of unequal size. Hence, similar to the asymmetric division of stem/progenitor cells, polarised positioning of the mitotic spindle functions to generate intrinsically asymmetric daughters of tip cell division.

TC division generates daughters with distinct Vegfr activity.

Further dissection of the computational model indicated that the distinct motilities of TC daughters observed in control and *dll4* knockdown embryos could largely be recapitulated upon the cell-size dependent asymmetric partitioning of *vegfr* mRNA (Supplementary Fig. 4c-h), but not by even severe asymmetries in Vegfr protein or cell area. These observations were a consequence of longer half-life of *vegfr* mRNA versus Vegfr protein[22-24] (see Methods). Hence, the model predicted that asymmetries in cell size might regulate cell motility by differentially partitioning Vegfr signalling components to generate daughters with differential Vegfr activity. Consistent with this model prediction, live-cell imaging of dividing TCs followed by flash-fixation on ice and immunofluorescence staining for phosph-p44/42 mitogen-activated protein kinase (pErk), a key downstream component of the Vegfr pathway[25-29], revealed that divisions generated daughters with differential levels of Vegfr signalling (fig. 5). Firstly, live-cell imaging coupled with immunofluorescence staining demonstrated that leading TCs contained significantly more pErk than adjacent SCs or cells residing in the DA (Fig, 5a-c). Inhibition of Vegfr abrogated pErk staining, confirming that endothelial Erk phosphorylation was Vegfr-dependent (Fig. 5d). Moreover, cells possessing higher pErk levels were frequently more motile than adjacent cells and maximal rates of motility were observed in cells containing pErk at TC levels or above (Fig. 5b, e). Hence, the differential motilities of TCs and SCs correlated with distinct levels of Vegfr activity.

Importantly, movies in which TC divisions were captured shortly prior to fixation indicated that distal daughters consistently displayed higher Vegfr-dependent pErk levels relative to proximal daughters (Fig. 5f). Furthermore, capture of mitotic TCs at the point at which they first split to form distinct daughters revealed that distal daughters asymmetrically acquired higher pErk levels (Fig. 5g). Quantification demonstrated that pErk levels were low during division when only one dividing TC was distinguished, likely due to mitotic disruption of Vegfr endocytosis and/or recycling[30-32] (Fig. 5h). However, when two daughter TCs were first distinguished, each immediately displayed differential Vegfr signalling, with distal daughters re-establishing TC-like activity and proximal daughters adopting SC-like levels (Fig. 5h). Hence, asymmetric division introduce heterogeneity that self-generates daughters with distinct levels of Vegfr activity.

Differential partitioning of filopodia does not drive asymmetric division

Consistent with these observations, the larger distal daughters of TC division possessed more Vegfr-dependent filopodial protrusions[3] than smaller proximal daughters (Fig. 4a; Supplementary Fig. 6). In agreement with previous work, the disruption of filopodia formation did not impact TC guidance[33], but also did not disrupt asymmetries in TC daughter motility, which remained dependent on cell size (Supplementary Fig. 6c to j). However, the tight correlation of Vegfr-induced filopodia numbers with daughter cell motility (Supplementary Fig. 6b) further indicated that underlying asymmetries in Vegfr activity drive differential post-mitotic motility.

***Kdrl* mRNA is asymmetrically partitioned during TC division**

Modelling of asymmetric tip cell division suggested that differential size-dependent partitioning of Vegfr signalling components, such as *vegfr* mRNA, generates daughters with distinct Vegfr signalling levels. Consistent with this model prediction, live-cell imaging and fluorescent *in-situ* hybridisation (FISH) revealed that mRNA encoding *kinase insert domain receptor-like* (*kdrl*) mRNA, a key *VEGFR* orthologue in zebrafish[34,35], was asymmetrically partitioned in TC daughters (Fig. 5i, j). Interestingly, prior to division *kdrl* mRNA was localised at distal peri-nucelar sites in migrating TCs (Supplementary Fig. 6k-p), suggesting roles for mRNA targeting in Vegfr function. However, this localisation of *kdrl* mRNA was disrupted during mitosis and appeared more homogenously localised, similar to *egfp* mRNA. Consequently, during division both *kdrl* mRNA and *egfp* mRNA were asymmetrically partitioned, with distal daughters inheriting 1.7 to 1.9 times more mRNA than proximal daughters (Fig. 5j), suggesting global asymmetries in cellular components. Thus, asymmetric divisions generate daughters with differentially partitioned *kdrl* mRNA, discrete tip/stalk thresholds of pro-migratory Vegfr signalling and distinct tip/stalk motilities.

Vegfr asymmetry is required for daughter tip/stalk positioning

Finally, we aimed to determine whether post-mitotic Vegfr asymmetry mechanistically drives re-organisation of daughters into leading and trailing collectively migrating cells. Treatment of embryos with the pan-specific Vegfr inhibitor SU5416 at doses of 0.6 μM or above severely disrupted endothelial cell Vegfr signalling and pErk staining (Fig. 6a). However, a partial SU5416 dose of 0.3 μM attenuated pErk levels to approximately 60% of controls, reducing Vegfr activity in all sprouting cells to SC-like levels (Fig. 6a, b). Subsequent incubation with 0.3 μM SU5416 during division did not disrupt the

orientation of endothelial cell division but generated TC daughters that all displayed SC-like motilities (Fig. 6c, d and Supplementary Video 12). Hence, in the absence of differential Vegfr thresholds, TC daughters assumed symmetric motile behaviours. Similar results were also observed using the more selective Vegfr-2 inhibitor, ZM323881 (Fig. 6e, f). In contrast, SCs retained the ability to generate daughters with differential motilities (Fig. 6d, f). Moreover, in the presence of 0.3 μM SU5416 we noted that proximal daughters of TC divisions frequently and atypically assumed the TC position. In control or *dll4* knockdown embryos, distal TC daughters robustly maintained TC positioning and were only occasionally overtaken by proximal daughters (Fig. 6g, i, l and Supplementary Video 13). However, upon incubation with 0.3 μM SU5416 during division, TC positioning was randomised with either daughter capable of taking the lead (Fig. 6i, l). In contrast, competition between TC daughters and adjacent SCs was not affected by the presence of 0.3 μM SU5416. After TC division, proximal daughters in control embryos were occasionally overtaken by adjacent SCs (Fig. 6h, j and Supplementary Video 14), likely due to transiently elevated Vegfr activity observed in SCs residing adjacent to dividing TCs (Supplementary Fig. 6k). This shuffling behaviour was augmented by *dll4* knockdown, but was unaffected by partial Vegfr inhibition (Fig. 6j, l). Hence, SU5416-induced symmetric TC division selectively enhanced competition only between TC daughters and randomised assignment of tip-stalk positioning after division. Taken together, these data reveal that post-mitotic Vegfr asymmetry functions to instantly re-establish the tip-stalk hierarchy and maintain uninterrupted collective migration during proliferative growth.

DISCUSSION

Our results define a previously unidentified role for asymmetric cell division in the control of collective cell migration. In particular, we show that post-mitotic Vegfr heterogeneity self-generates leader-follower cell hierarchies that drive coordinated collective movements in angiogenesis (Fig. 6m). Generation of cell type diversity by asymmetric division remarkably mirrors the proposed role of mitosis in lymphatic progenitor emergence[36,37], suggesting a wider role for Vegfr asymmetry in divergent vascular fate choices. Furthermore, our observation of tip/stalk selection by asymmetric division redefines the current view that tip/stalk identity is exclusively specified by Dll4/Notch-dependent lateral inhibition. It was recently proposed that the temporal dynamics of Dll4/Notch-mediated lateral inhibition are too slow to account for many of the rapid, adaptive switches of cell identity observed during blood vessel branching[14]. Vegfr asymmetry may account for these observations, as self-organisation of daughters into leading/trailing cells is near instantaneous and eradicates the need to pause for re-specification of tip/stalk identity by lateral inhibition. As such, asymmetric divisions functionally integrate proliferation with seamless re-establishment of tip-stalk hierarchy to robustly maintain uninterrupted collective migration during tissue growth. Consequently, endothelial cell migration and angiogenesis are acutely temporally delayed in the absence of asymmetric divisions. Considering that maintenance of multicellular leader-follower polarity underlies all collectively migrating cell systems[38], asymmetric divisions may drive the integrated growth of multiple tissues during embryonic development, wound healing and cancer invasion.

References

1. Carmeliet, P. & Jain, R. K. Molecular mechanisms and clinical applications of angiogenesis. *Nature* **473,** 298–307 (2011).
2. Herbert, S. P. & Stainier, D. Y. R. Molecular control of endothelial cell behaviour during blood vessel morphogenesis. *Nat. Rev. Mol. Cell Biol.* **12,** 551–564 (2011).
3. Gerhardt, H. *et al.* VEGF guides angiogenic sprouting utilizing endothelial tip cell filopodia. *J. Cell Biol.* **161,** 1163–1177 (2003).
4. Ruhrberg, C. *et al.* Spatially restricted patterning cues provided by heparin-binding VEGF-A control blood vessel branching morphogenesis. *Genes Dev.* **16,** 2684–2698 (2002).
5. Siekmann, A. F. & Lawson, N. D. Notch signalling limits angiogenic cell behaviour in developing zebrafish arteries. *Nature* **445,** 781–784 (2007).
6. Hellström, M. *et al.* Dll4 signalling through Notch1 regulates formation of tip cells during angiogenesis. *Nature* **445,** 776–780 (2007).
7. Benedito, R. *et al.* Notch-dependent VEGFR3 upregulation allows angiogenesis without VEGF-VEGFR2 signalling. *Nature* **484,** 110–114 (2012).
8. Zarkada, G., Heinolainen, K., Makinen, T., Kubota, Y. & Alitalo, K. VEGFR3 does not sustain retinal angiogenesis without VEGFR2. *Proceedings of the National Academy of Sciences* **112,** 761–766 (2015).
9. Jakobsson, L. *et al.* Endothelial cells dynamically compete for the tip cell position during angiogenic sprouting. *Nat. Cell Biol.* **12,** 943–953 (2010).
10. Arima, S. *et al.* Angiogenic morphogenesis driven by dynamic and heterogeneous collective endothelial cell movement. *Development* **138,** 4763–

4776 (2011).

11. Ausprunk, D. H. & Folkman, J. Migration and proliferation of endothelial cells in preformed and newly formed blood vessels during tumor angiogenesis. *Microvascular Research* **14,** 53–65 (1977).

12. Schoors, S. *et al.* Fatty acid carbon is essential for dNTP synthesis in endothelial cells. *Nature* (2015). doi:10.1038/nature14362

13. Matsuda, M., Koga, M., Woltjen, K., Nishida, E. & Ebisuya, M. Synthetic lateral inhibition governs cell-type bifurcation with robust ratios. *Nat Commun* **6,** 6195 (2015).

14. Bentley, K., Harrington, K. & Regan, E. Can Active Perception Generate Bistability? Heterogeneous Collective Dynamics and Vascular Patterning. *ALIFE* 328–335 (2014). doi:10.7551/978-0-262-32621-6-ch053

15. Sauteur, L. *et al.* Cdh5/VE-cadherin Promotes Endothelial Cell Interface Elongation via Cortical Actin Polymerization during Angiogenic Sprouting. *Cell Rep* **9,** 504–513 (2014).

16. Zeng, G. *et al.* Orientation of endothelial cell division is regulated by VEGF signaling during blood vessel formation. *Blood* **109,** 1345–1352 (2007).

17. Aydogan, V. *et al.* Endothelial cell division in angiogenic sprouts of differing cellular architecture. *Biol Open* **4,** 1259–1269 (2015).

18. Knoblich, J. A. Mechanisms of asymmetric stem cell division. *Cell* **132,** 583–597 (2008).

19. Li, R. The art of choreographing asymmetric cell division. *Dev. Cell* **25,** 439–450 (2013).

20. Bentley, K. *et al.* The role of differential VE-cadherin dynamics in cell

rearrangement during angiogenesis. *Nat. Cell Biol.* **16,** 309–321 (2014).

21. Villefranc, J. A. *et al.* A truncation allele in vascular endothelial growth factor c reveals distinct modes of signaling during lymphatic and vascular development. *Development* **140,** 1497–1506 (2013).

22. Meissner, M. *et al.* Microtubule-targeted drugs inhibit VEGF receptor-2 expression by both transcriptional and post-transcriptional mechanisms. *J. Invest. Dermatol.* **128,** 2084–2091 (2008).

23. Meissner, M. *et al.* Down-regulation of vascular endothelial growth factor receptor 2 is a major molecular determinant of proteasome inhibitor-mediated antiangiogenic action in endothelial cells. *Cancer Research* **69,** 1976–1984 (2009).

24. Murakami, M. *et al.* FGF-dependent regulation of VEGF receptor 2 expression in mice. *J. Clin. Invest.* **121,** 2668–2678 (2011).

25. Mavria, G. *et al.* ERK-MAPK signaling opposes Rho-kinase to promote endothelial cell survival and sprouting during angiogenesis. *Cancer Cell* **9,** 33–44 (2006).

26. Alavi, A., Hood, J. D., Frausto, R., Stupack, D. G. & Cheresh, D. A. Role of Raf in vascular protection from distinct apoptotic stimuli. *Science* **301,** 94–96 (2003).

27. Shin, M. *et al.* Vegfa signals through ERK to promote angiogenesis, but not artery differentiation. *Development* dev.137919 (2016). doi:10.1242/dev.137919

28. Shin, M. *et al.* Vegfc acts through ERK to induce sprouting and differentiation of trunk lymphatic progenitors. *Development* dev.137901 (2016). doi:10.1242/dev.137901

29. Nagasawa-Masuda, A. & Terai, K. ERK activation in endothelial cells is a novel

marker during neovasculogenesis. *Genes Cells* (2016). doi:10.1111/gtc.12438

30. Horowitz, A. & Seerapu, H. R. Regulation of VEGF signaling by membrane traffic. *Cellular Signalling* **24,** 1810–1820 (2012).

31. Fielding, A. B., Willox, A. K., Okeke, E. & Royle, S. J. Clathrin-mediated endocytosis is inhibited during mitosis. *Proceedings of the National Academy of Sciences* **109,** 6572–6577 (2012).

32. Boucrot, E. & Kirchhausen, T. Endosomal recycling controls plasma membrane area during mitosis. *Proc. Natl. Acad. Sci. U.S.A.* **104,** 7939–7944 (2007).

33. Phng, L.-K., Stanchi, F. & Gerhardt, H. Filopodia are dispensable for endothelial tip cell guidance. *Development* **140,** 4031–4040 (2013).

34. Covassin, L. D., Villefranc, J. A., Kacergis, M. C., Weinstein, B. M. & Lawson, N. D. Distinct genetic interactions between multiple Vegf receptors are required for development of different blood vessel types in zebrafish. *Proc. Natl. Acad. Sci. U.S.A.* **103,** 6554–6559 (2006).

35. Bussmann, J., Lawson, N., Zon, L., Schulte-Merker, S.Zebrafish Nomenclature Committee. Zebrafish VEGF receptors: a guideline to nomenclature. *PLoS Genet* **4,** e1000064 (2008).

36. Nicenboim, J. *et al.* Lymphatic vessels arise from specialized angioblasts within a venous niche. *Nature* (2015). doi:10.1038/nature14425

37. Koltowska, K. *et al.* Vegfc Regulates Bipotential Precursor Division and Prox1 Expression to Promote Lymphatic Identity in Zebrafish. *Cell Rep* **13,** 1828–1841 (2015).

38. Friedl, P. & Gilmour, D. Collective cell migration in morphogenesis, regeneration and cancer. *Nat. Rev. Mol. Cell Biol.* **10,** 445–457 (2009).

39. Blum, Y. *et al.* Complex cell rearrangements during intersegmental vessel sprouting and vessel fusion in the zebrafish embryo. *Dev. Biol.* **316,** 312–322 (2008).

40. Fukuhara, S. *et al.* Visualizing the cell-cycle progression of endothelial cells in zebrafish. *Dev. Biol.* (2014). doi:10.1016/j.ydbio.2014.06.015

41. Jin, S. W. Cellular and molecular analyses of vascular tube and lumen formation in zebrafish. *Development* **132,** 5199–5209 (2005).

42. Chi, N. C. *et al.* Foxn4 directly regulates tbx2b expression and atrioventricular canal formation. *Genes Dev.* **22,** 734–739 (2008).

43. Herbert, S. P. *et al.* Arterial-venous segregation by selective cell sprouting: an alternative mode of blood vessel formation. *Science* **326,** 294–298 (2009).

44. Herbert, S. P., Cheung, J. Y. M. & Stainier, D. Y. R. Determination of Endothelial Stalk versus Tip Cell Potential during Angiogenesis by H2.0-like Homeobox-1. *Curr. Biol.* **22,** 1789–1794 (2012).

45. De Bock, K. *et al.* Role of PFKFB3-driven glycolysis in vessel sprouting. *Cell* **154,** 651–663 (2013).

46. Steketee, M. B. & Tosney, K. W. Three functionally distinct adhesions in filopodia: shaft adhesions control lamellar extension. *Journal of Neuroscience* **22,** 8071–8083 (2002).

47. Bentley, K., Gerhardt, H. & Bates, P. A. Agent-based simulation of notch-mediated tip cell selection in angiogenic sprout initialisation. *J. Theor. Biol.* **250,** 25–36 (2008).

48. Le Guen, L. *et al.* Ccbe1 regulates Vegfc-mediated induction of Vegfr3 signaling during embryonic lymphangiogenesis. *Development* **141,** 1239–1249 (2014).

Acknowledgements We thank B. M. Hogan and N. D. Lawson for advice regarding the pErk staining protocol, and B. Plusa, M. Baron, K. Dorey, T. Millard and C. Thompson for critical reading of the manuscript. S.P.H. is a Wellcome Trust Research Career Development Fellow and is funded by the BBSRC (Ref. BB/N013174/1) and BHF (PG/16/2/31863). K.B. is funded by BIDMC and NSF (Ref. 1517390). K.I.H. is supported by institutional training grant T32 HL07893 from the NHLBI of the NIH.

Author Contributions S.P.H. designed the research and wrote the paper, S.P.H., G.C., H.E.C. and D.J.P. performed the experiments and analysed the data, K.B. and K.I.H. developed the theoretical model. S.C. performed statistical analysis of the data. All authors discussed the results and implications and commented on the manuscript.

Competing Financial Interests The authors declare no competing financial interests.

Figure Legends

Figure 1: Endothelial cell division generates daughters with distinct behaviours. (**a** and **b**) Time-lapse images of individual lyn-mCherry expressing tip (**a**; cell 1) or stalk (**b**; cell 2) cells in sprouting ISVs of *Tg(kdrl:nlsEGFP)*^{zf109} embryos from around 22 hours post-fertilisation (hpf). (**c** and **d**) Quantification of the dorsal movement of cell nuclei and the top, bottom and centre of migrating tip (**c**; *n*=8 ISVs, 7 embryos) or stalk (**d**; *n*=9 ISVs, 8 embryos) cells. (**e** and **f**) Quantification of the averaged motility of all tracked endothelial cell nuclei from 22 hpf (**e**, *n*=136 ISVs, 34 embryos) or of tracked nuclei from ISVs in which TCs or SCs did or did not divide (**f**, *n*=83 ISVs, 1 no div; *n*=51 ISVs, 1 div; *n*=58 ISVs, 2 no div; *n*=42 ISVs; 2 div, 34 embryos). In **f**, If a TC or SC divided, only the distal-most daughter continued to be tracked. (**g** and **h**) Time-lapse images of sprouting ISVs from 0.3h prior to either TC division (**g**) or SC division (**h**) in control *Tg(kdrl:nlsEGFP)*^{zf109} embryos. Brackets indicate dividing cells. Nuclei are pseudocoloured according to their initial position. (**i**) Quantification of the dorsal movement of daughter cells following TC and SC division in control embryos (**i**, *n*=43 ISVs, 1.1/1.2; *n*=41 ISVs, 2.1/2.2, 34 embryos). Dashed lines represent trend-lines of endothelial cell motilities from **e**. (**j**) Time-lapse images of an individual lyn-mCherry expressing TC in a sprouting ISV of a *Tg(kdrl:nlsEGFP)*^{zf109} embryo from 22 hpf. Bracket indicates the point of TC division. (**k** and **l**) Quantification of the dorsal movement of cell nuclei and the top, bottom and centre of the migrating distal daughter cell (**k**; cell 1.1) or proximal daughter cell (**l**; cell 1.2) following TC division. Brackets indicate the point of TC division. Source data for **c**, **d**, **e**, **f** and **i** are shown in Supplementary Table 2. Error bars: mean ± SEM. **P*<0.0001, two way ANOVA test. Scale bars, 25 μm.

Figure 2: Post-mitotic asymmetry is independent of Dll4-Notch signalling. (**a**) Time-lapse images of sprouting ISVs from 22 hpf in *Tg(kdrl:nlsEGFP)*^{zf109} embryos upon *dll4* knockdown (*dll4* KD). Nuclei are pseudocoloured according to their initial position. Arrowheads indicate a super-motile SC. (**b**) Quantification of the dorsal movement of tracked endothelial cell nuclei from 22 hpf upon dll4 knockdown (*n*=80 ISVs, 23 embryos). Dashed lines represent endothelial cells motilities from **Fig. 1e**. In the absence of dll4 SCs adopt TC-like motilities. (**c**) Quantification of the total number of cells per ISV at 32.5 hpf, number of mitotic TCs or SCs per ISV, position of TC or SC divisions and the time of TC or SC divisions in control or dll4 knockdown embryos following live-cell imaging from 22 to 32.5 hpf (*n*=70 ISVs, 18 embryos, control; *n*=76 ISVs, 23 embryos, *dll4* KD). More endothelial cells sprout into ISVs and more SC divisions are observed in the absence of dll4. (**d**, **e**) Time-lapse images of sprouting ISVs from 0.3h prior to either TC division (**d**) or SC division (**e**) in *dll4* knockdown *Tg(kdrl:nlsEGFP)*^{zf109} embryos. Brackets indicate dividing cells. Nuclei are pseudocoloured according to their initial position. (**f**) Quantification of the dorsal movement of daughter cells following TC and SC division upon *dll4* knockdown (*n*=33 ISVs, 17 embryos, 1.1/1.2; *n*=29 ISVs, 16 embryos, 2.1/2.2) embryos. Dashed lines represent trend-lines of endothelial cell motilities from **Fig. 1e**. (**g** and **h**) Daughter cell behaviour following TC or SC division in control (**g**) or *dll4* knockdown (**h**) vessels. Source data for **b** and **f** are shown in Supplementary Table 2. Error bars: mean ± SEM. **P*<0.0001, two way ANOVA test. †P<0.05 control versus dll4 knockdown. ***P*<0.05 *dll4* KD 1.2 versus control 1.2 from **Fig. 1i**. Unpaired two-tailed Student's *t* test. Scale bars, 25 μm.

Figure 3: *in silico* and *in vivo* prediction of post-mitotic cell size asymmetry. (**a** and **b**) MemAgent-Spring model simulations of either symmetric (**a**) or asymmetric (**b)** TC divisions (*n*=10). Arrows and arrowheads indicate periods of either mutual activation or repression of TC daughters, respectively. (**c**) Photo-conversion and post-mitotic inheritance of rEos during TC division. (**d**) Images of an ISV in a *Tg(kdrl:nlsEos)*^{ncv6} embryo prior to or following irradiation with 405 nm light and quantification of the relative stability of TC rEos fluorescence versus gEos, which increases over time (*n*=8 cells). (**e** and **f**) Time-lapse images of rEos fluorescence in a dividing photo-converted TC (**e**) and quantification of rEos levels inherited by each TC daughter, as well as the total rEos fluorescence present before (cell 1) and after (cells 1.1 + 1.2) TC division (**f**, *n*=15 dividing TCs from 7 embryos). Bracket in **e** indicates TC division. Error bars: mean ± SEM. **P*<0.01 1.1 versus 1.2. Unpaired two-tailed Student's *t* test. Scale bars, 25 μm.

Figure 4: TC division generates daughter cell size asymmetry. (**a** and **b**) Time-lapse images of a dividing lyn-mCherry-and nlsEGFP-expressing TCs and quantification of either cell size (**a**; *n*=14 pre-div TCs; *n*=13 post-div TCs, from 12 embryos) or cell volume (**b**; *n*= 5 dividing TCs from 5 embryos) both before (cell 1) and directly after (cell 1.1 and cell 1.2) TC division. Bracket and arrowheads indicate a mitotic TC and the *de novo* interface between daughter cells, respectively. (**c**) Quantification of the dorsal movement of TC daughters of the indicated sizes (*n*=22 cells from 9 embryos). (**d**) Correlation of the size of individual TC daughters with their rate of post-mitotic motility (*P*<0.001. Pearson's correlation. R^2=0.56. *n*=24 cells from 11 embryos). (**e**)

Correlation of the difference in size between TC daughters (distal cell size – proximal cell size) with their differences in cell motility (distal cell motility – proximal cell motility; $P<0.02$. Pearson's correlation. $R^2=0.46$. $n=12$ dividing cells from 11 embryos). (**f**) Time-lapse images of an individual dividing lyn-mCherry and α-tubulin-GFP-expressing tip cell in a *Tg(kdrl:ras-mCherry)*^{s896} embryo, and quantification of spindle movement during mitosis (NEB, nuclear envelope breakdown; ana., anaphase; tel., telophase; $n=8$ dividing cells from 8 embryos). Error bars: mean ± SEM. *$P<0.05$ 1.1 versus 1.2. **$P<0.01$ versus anaphase. Unpaired two-tailed Student's *t* test. Scale bars, 25 μm.

Figure 5: TC division asymmetrically partitions Vegfr activity. (**a**, **b**, **f**, **g**) Time-lapse images of nlsEGFP-expressing sprouting ISVs and localisation of pErk (red). Nuclei are pseudocoloured according to their initial position. Brackets in **f** and **g** indicate dividing TCs. The highly motile TC in **b** exhibits much higher levels of Vegfr signaling activity adjacent SCs. The distal daughters of TC division in **f** and **g** exhibit higher levels of Vegfr signaling activity than the proximal daughter. (**c**) Quantification of pErk fluorescence intensity at the indicated positions. TCs and SCs display distinct levels of Vegfr-dependent pErk ($n=44$ embryos). (**d**) Quantification of TC pErk levels in *Tg(kdrl:nlsEGFP)*^{zf109} embryos upon incubation with DMSO, 2 μM SU5416, 5 μM DMH4, 1 μM Ki8751 and 5 μM ZM323881 ($n=9$ embryos, DMSO, SU5416, DMH4, Ki8751; $n=6$ embryos, ZM323881). (**e**) Correlation between pErk levels and endothelial cell motility (n=21, 36, 50, 68, 48 and 40 cells for <5, <10, <15, <20, <25 and >25, respectively, from 14 embryos). (**h**) Quantification of pErk levels during and after TC division. Distal daughters of TC divisions exhibit higher levels of Vegfr signaling

activity than proximal daughters (*n*=85 no-div TCs; *n*=9 during div., 0h div.and 0.3h div.; *n*=18 >0.3h div., 44 embryos). (**i**) Time-lapse images of a dividing nlsEGFP-expressing TC and localisation of ZO-1 protein (white), *kdrl* mRNA (red) and e*gfp* mRNA (green). Bracket, white arrowheads and red arrowheads indicate the mitotic TC, the *de novo* daughter cell-cell junction and the pre-existing TC-SC junction, respectively. White lines indicate the position of ZO-1 positive cell-cell junctions. (**j**) Quantification of *kdrl* and *egfp* mRNA segregation in the distal-most versus the proximal-most daughters of TC division (*n*=19 TC divisions, 16 embryos, *kdrl*; *n*=13 TC divisions, 10 embryos, *egfp*). Error bars: mean ± SEM. **P*<0.05 versus 1.2. ***P*<0.001 versus 1. †*P*<0.05 versus 4. ††P<0.001 versus DMSO-treated TC. ***P<0.05 versus <5 pERK intensity. Unpaired two-tailed Student's *t* test. Scale bars, 25 μm.

Figure 6: Disruption of Vegfr asymmetry randomises daughter tip/stalk positioning. (**a** and **b**) Quantification (**a**) and localisation (**b**) of pErk levels in endothelial cells of *Tg(kdrl:nlsEGFP)*^{zf109} embryos upon incubation with DMSO or the indicated concentration of SU5416. 0.3 μM SU5416 reduces TC pErk to SC levels (*n*=129 ISVs, 17 embryos, DMSO; *n*=109 ISVs, 17 embryos, 0.3 μM; *n*=113 ISVs, 18 embryos, 0.6 μM). (**c**, **g** and **h**) Time-lapse images of sprouting ISVs from 0.3 h prior to TC division in 0.3 μM SU5416-treated (**c**) or control (**g** and **h**) embryos. Nuclei are pseudocoloured according to their initial position. Brackets indicate dividing TCs. Open arrowheads indicate the position of a normal 1.1 TC daughters following division. (**d**) Quantification of the dorsal movement of daughter endothelial cells following TC and SC division in 0.3 μM SU5416-treated embryos (*n*=54 ISVs, 1.1/1.2; *n*=10 ISVs,

2.1/2.2, 22 embryos). (**e**) Quantification of pErk levels in endothelial cells upon incubation with DMSO or the indicated concentration of ZM323881 (*n*=42 ISVs, 8 embryos). 80 nM ZM323881 reduces TC pErk to SC levels. (**f**) Quantification of the dorsal movement of daughter endothelial cells following TC and SC division in 80 nM ZM323881-treated embryos (*n*=38 ISVs, 1.1/1.2; *n*=11 ISVs, 2.1/2.2, 17 embryos). (**i**) Quantification of the number of distal 1.1 TC daughters overtaken by proximal 1.2 TC daughters following division (*n*=59 divisions, 26 embryos, control; *n*=48 divisions, 20 embryos, *dll4* MO; *n*=48 divisions, 22 embryos, SU5416). (**j**) Quantification of the number of proximal 1.2 TC daughters overtaken by adjacent SCs following TC division (*n*=57 divisions, 26 embryos, control; *n*=38 divisions, 20 embryos, *dll4* MO; *n*=65 divisions, 24 embryos, SU5416). (**k**) Quantification of pErk levels in non-dividing TCs, SCs adjacent to TCs that do not divide, SCs adjacent to a dividing TC or SCs adjacent to a TC that had previously divided. SC pErk levels rise during division of an adjacent TC (*n*=71 cells, 28 embryos, cell 1 and no div. 2; *n*=11 cells, 11 embryos, during div. 2; *n*=14 cells, 8 embryos, after div. 2). (**l**) Endothelial cell rearrangements following TC division. (**m**) Model summarising the mechanisms of asymmetric division in angiogenesis. Source data for **d** and **f** are shown in Supplementary Table 2. Error bars: mean ± SEM. **P*<0.001 versus DMSO 1. ***P*<0.001 versus control. †P<0.001 versus 1. ‡P<0.05 versus 2 no-division. Unpaired two-tailed Student's t test. Scale bars, 25 μm.

Figure 1

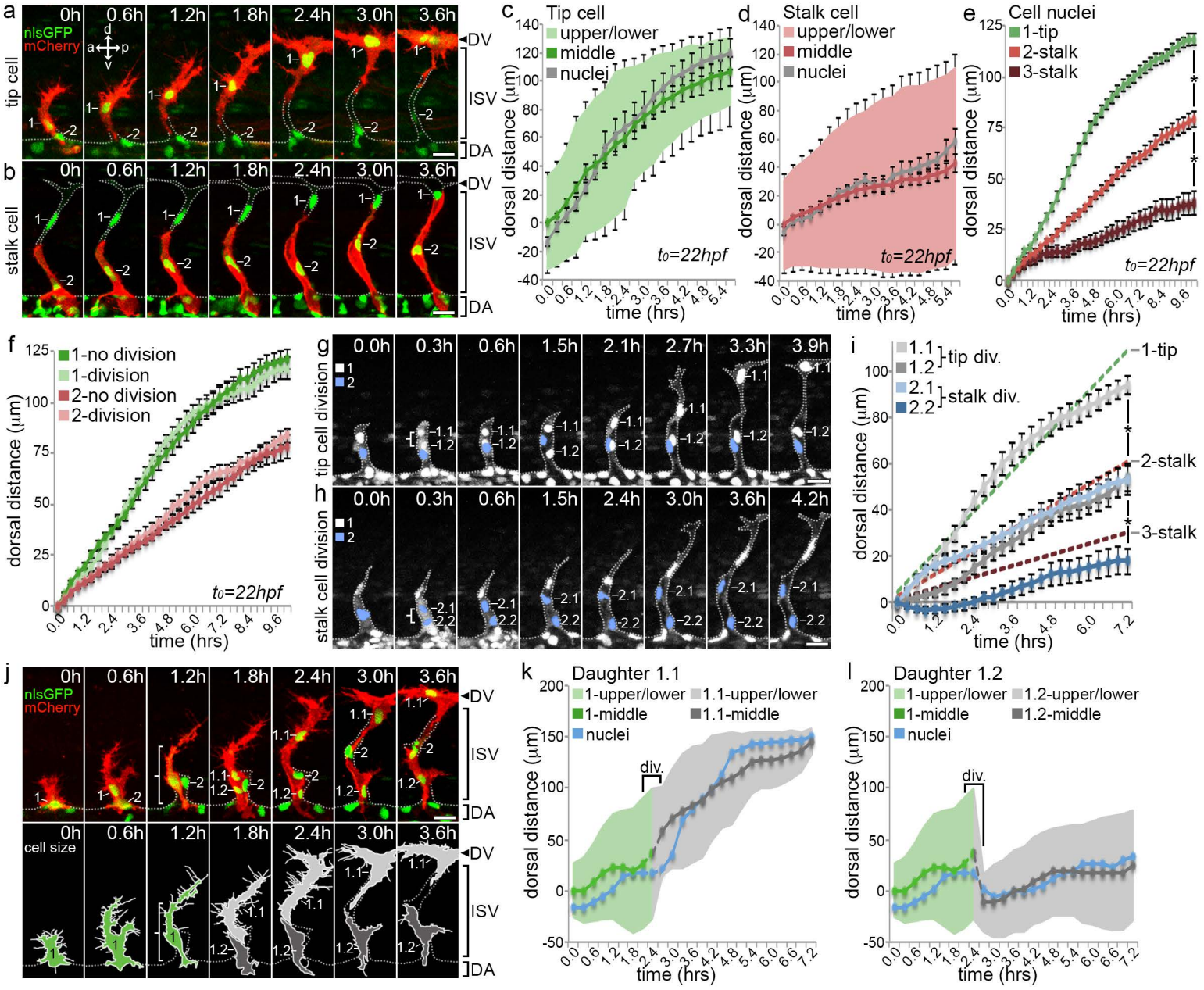
a
0h
0.6h
1.2h
1.8h
2.4h
3.0h
3.6h
nlsGFP
mCherry
tip cell
DV
ISV
DA
b
stalk cell
c
Tip cell
upper/lower
middle
nuclei
dorsal distance (μm)
time (hrs)
t0=22hpf
d
Stalk cell
e
Cell nuclei
1-tip
2-stalk
3-stalk
f
1-no division
1-division
2-no division
2-division
g
tip cell division
h
stalk cell division
i
tip div.
stalk div.
j
cell size
k
Daughter 1.1
1-upper/lower
1.1-upper/lower
1-middle
1.1-middle
div.
l
Daughter 1.2
1.2-upper/lower
1.2-middle

Figure 2

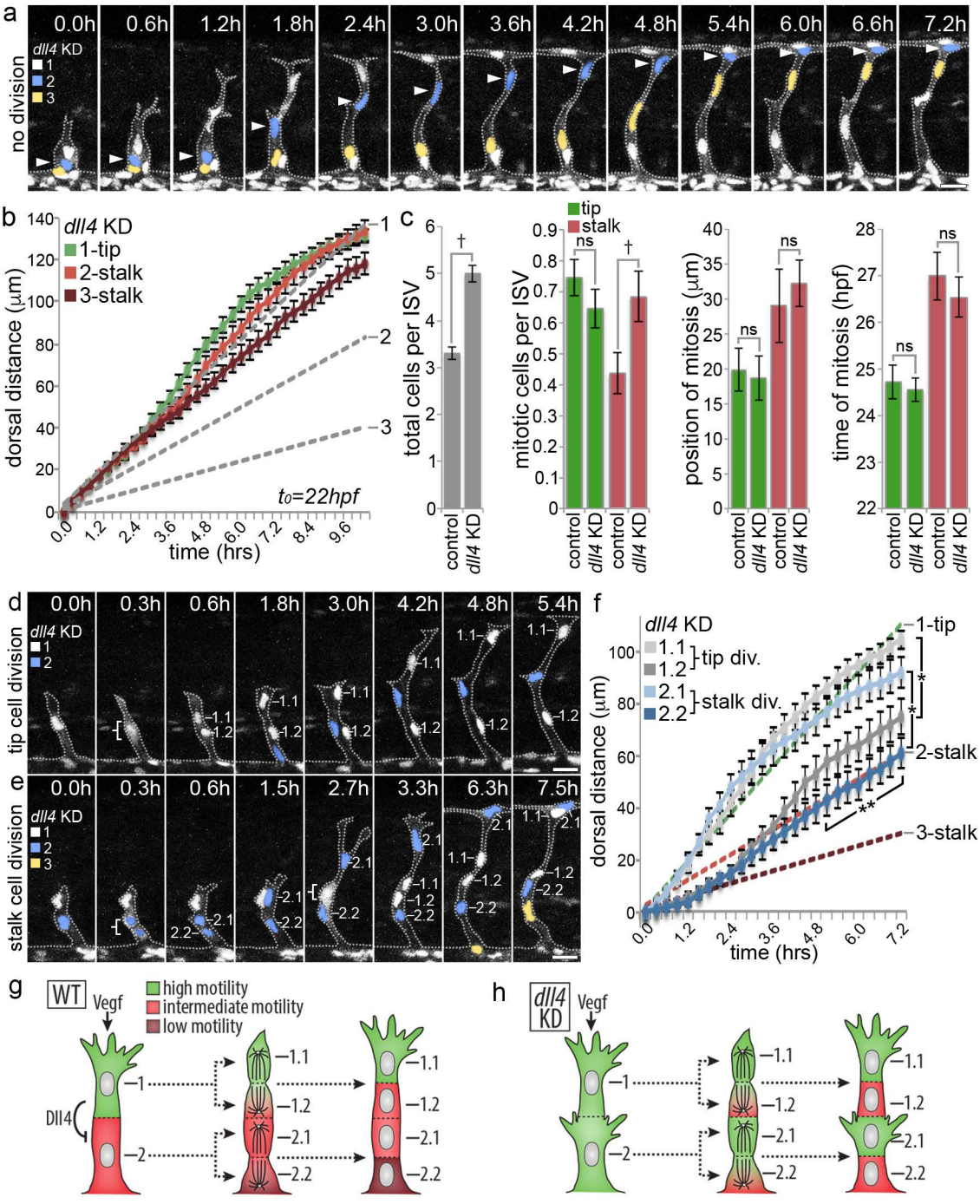
a
0.0h
0.6h
1.2h
1.8h
2.4h
3.0h
3.6h
4.2h
4.8h
5.4h
6.0h
6.6h
7.2h
dll4 KD
1
2
3
no division
b
dll4 KD
1-tip
2-stalk
3-stalk
dorsal distance (μm)
time (hrs)
t0=22hpf
1
2
3
c
total cells per ISV
tip
stalk
mitotic cells per ISV
position of mitosis (μm)
time of mitosis (hpf)
ns
†
control
dll4 KD
d
tip cell division
e
stalk cell division
f
dll4 KD
1.1
1.2
2.1
2.2
tip div.
stalk div.
1-tip
2-stalk
3-stalk
dorsal distance (μm)
time (hrs)
g
WT
Vegf
high motility
intermediate motility
low motility
Dll4
h
dll4 KD
Vegf

Figure 3

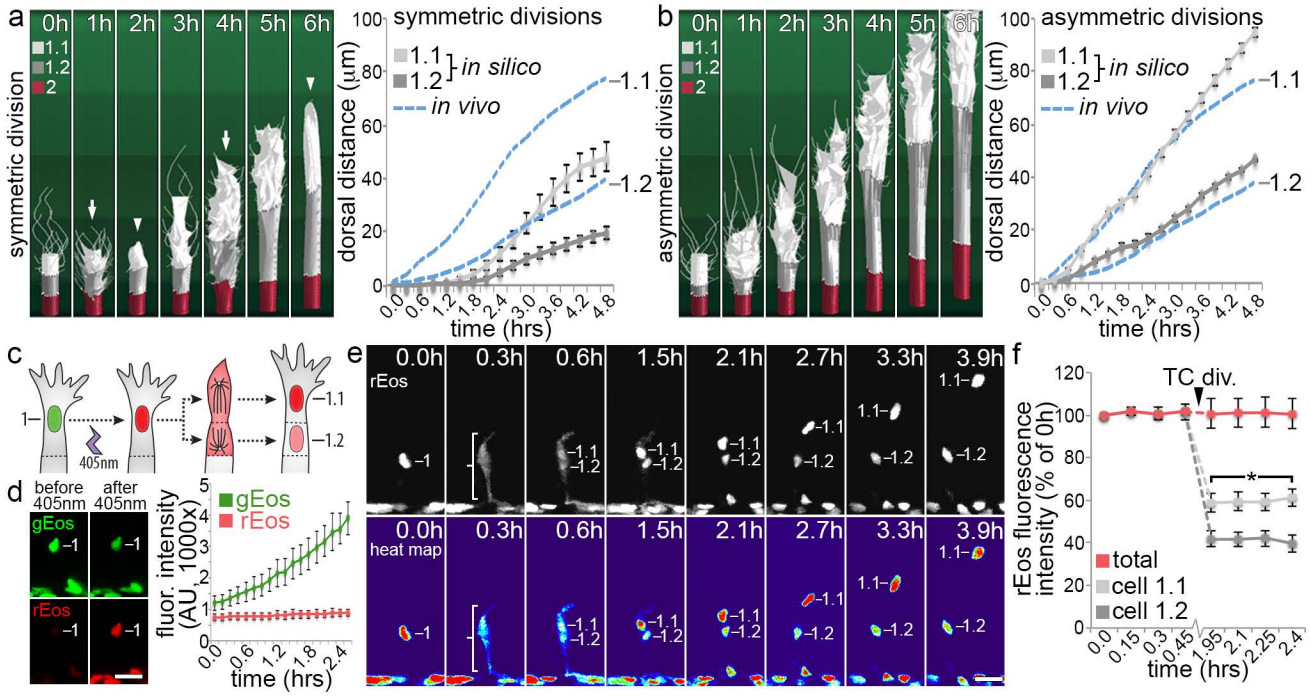
a
0h 1h 2h 3h 4h 5h 6h
1.1
1.2
2
symmetric division
symmetric divisions
dorsal distance (μm)
in silico
in vivo
1.1
1.2
time (hrs)
b
asymmetric division
asymmetric divisions
c
405nm
d
before 405nm
after 405nm
gEos
rEos
fluor. intensity (AU, 1000x)
e
rEos
heat map
f
TC div.
rEos fluorescence intensity (% of 0h)
total
cell 1.1
cell 1.2

Figure 4

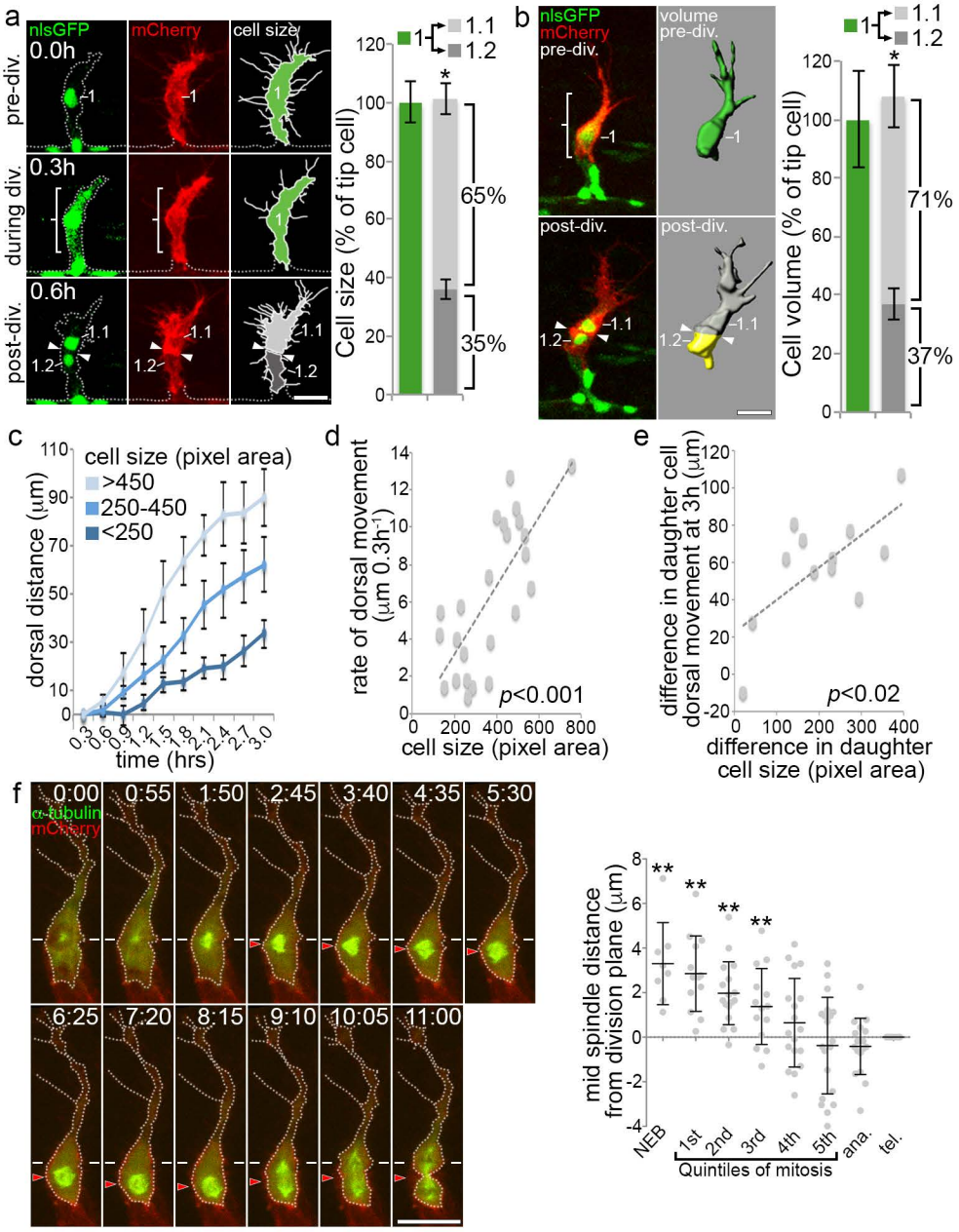
a
nlsGFP
mCherry
cell size
pre-div.
during div.
post-div.
0.0h
0.3h
0.6h
1
1.1
1.2
Cell size (% of tip cell)
65%
35%
b
nlsGFP
mCherry
pre-div.
volume
pre-div.
post-div.
Cell volume (% of tip cell)
71%
37%
c
cell size (pixel area)
>450
250-450
<250
dorsal distance (μm)
time (hrs)
d
rate of dorsal movement (μm 0.3h-1)
p<0.001
cell size (pixel area)
e
difference in daughter cell dorsal movement at 3h (μm)
p<0.02
difference in daughter cell size (pixel area)
f
α-tubulin
mCherry
0:00
0:55
1:50
2:45
3:40
4:35
5:30
6:25
7:20
8:15
9:10
10:05
11:00
mid spindle distance from division plane (μm)
NEB
1st
2nd
3rd
4th
5th
ana.
tel.
Quintiles of mitosis

Figure 5

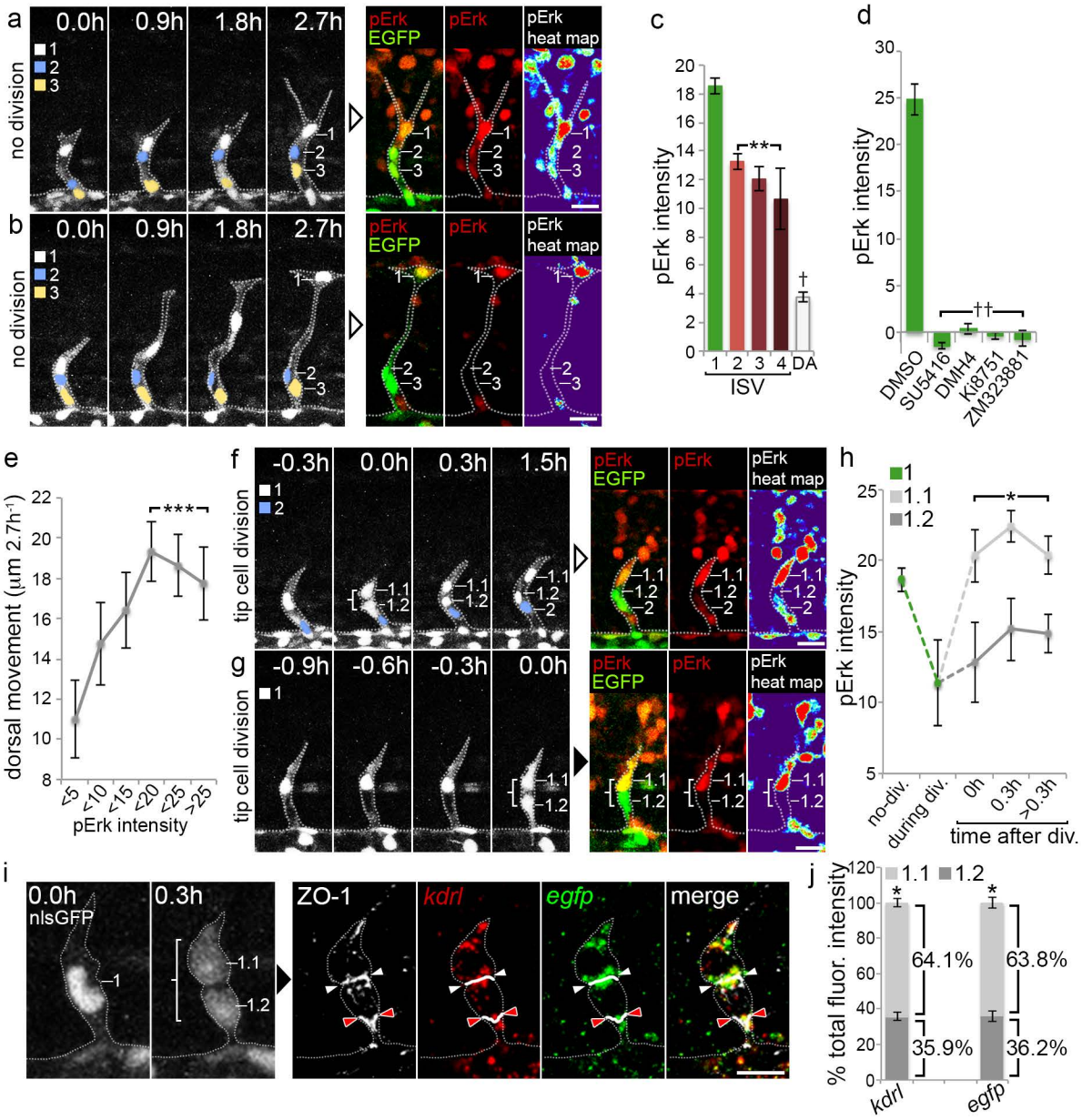
a
0.0h
0.9h
1.8h
2.7h
no division
pErk EGFP
pErk
pErk heat map
b
c
pErk intensity
ISV
DA
d
DMSO
SU5416
DMH4
Ki8751
ZM323881
e
dorsal movement (μm 2.7h-1)
pErk intensity
f
-0.3h
0.0h
0.3h
1.5h
tip cell division
g
-0.9h
-0.6h
-0.3h
0.0h
h
no-div.
during div.
0h
0.3h
>0.3h
time after div.
i
nlsGFP
ZO-1
kdrl
egfp
merge
j
% total fluor. intensity
64.1%
35.9%
63.8%
36.2%

Figure 6

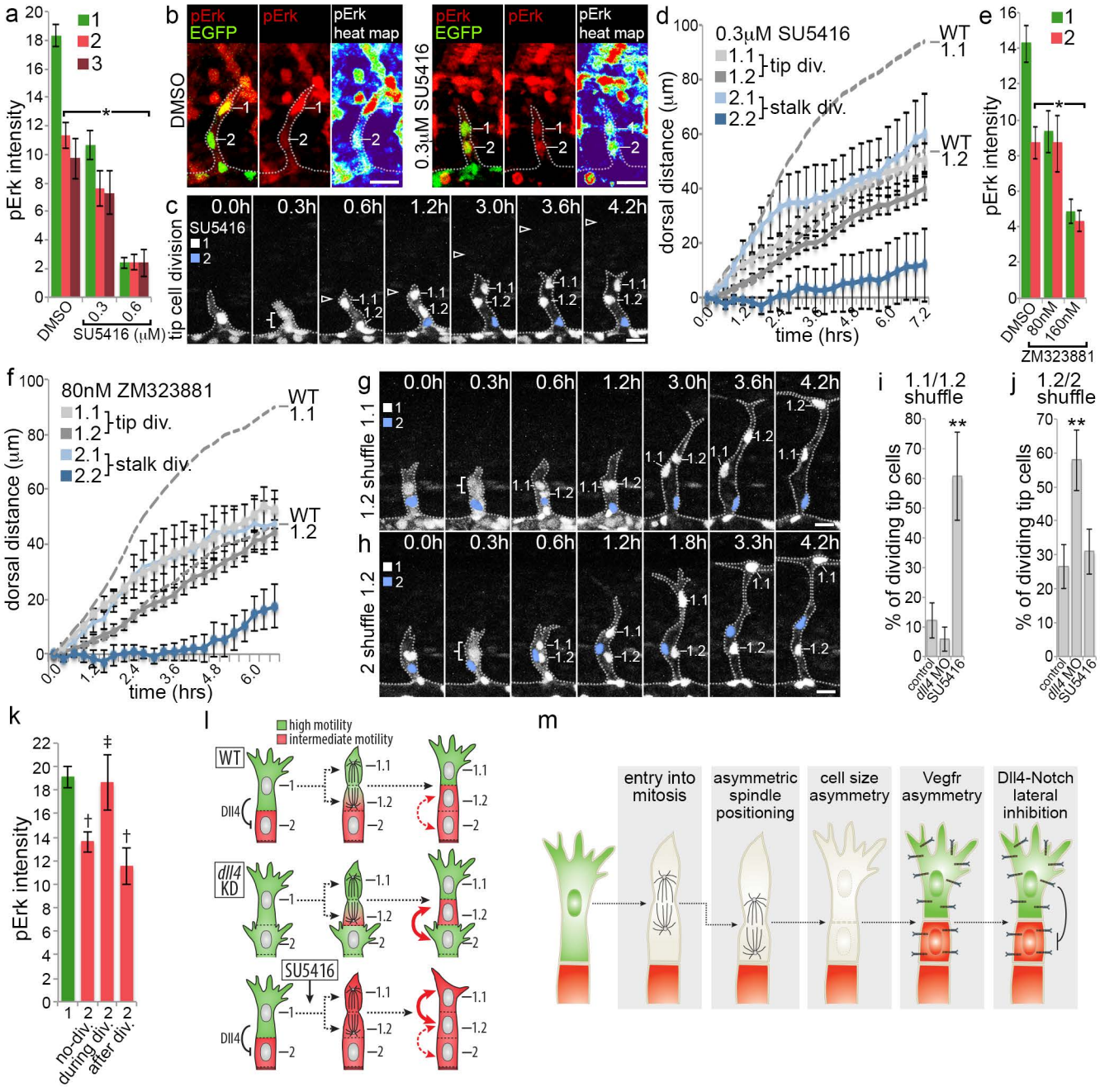
a
pErk intensity
DMSO
0.3
0.6
SU5416 (μM)
b
pErk
EGFP
pErk
pErk
heat map
DMSO
0.3μM SU5416
c
tip cell division
SU5416
0.0h
0.3h
0.6h
1.2h
3.0h
3.6h
4.2h
d
0.3μM SU5416
tip div.
stalk div.
WT
1.1
WT
1.2
dorsal distance (μm)
time (hrs)
e
pErk intensity
DMSO
80nM
160nM
ZM323881
f
80nM ZM323881
tip div.
stalk div.
WT
1.1
WT
1.2
dorsal distance (μm)
time (hrs)
g
1.2 shuffle 1.1
h
2 shuffle 1.2
0.0h
0.3h
0.6h
1.2h
1.8h
3.0h
3.6h
4.2h
i
1.1/1.2
shuffle
% of dividing tip cells
control
dll4 MO
SU5416
j
1.2/2
shuffle
% of dividing tip cells
control
dll4 MO
SU5416
k
pErk intensity
no-div.
during div.
after div.
l
high motility
intermediate motility
WT
dll4
KD
SU5416
Dll4
m
entry into
mitosis
asymmetric
spindle
positioning
cell size
asymmetry
Vegfr
asymmetry
Dll4-Notch
lateral
inhibition

Methods

Zebrafish strains and husbandry.

Establishment and characterisation of the *Tg(kdrl:nlsEGFP)*^{zf109}, *Tg(kdrl:nlsEos)*^{ncv6}, *Tg(kdrl:ras-mCherry)*^{s896} and *Tg(kdrl:GFP)*^{s843} transgenic lines have been described elsewhere[39-42]. Embryos and adults were maintained under standard laboratory conditions as described previously[43] and were approved by the University of Manchester Ethical Review Board and performed according to UK Home Office regulations. For experiments, embryos were not selected for gender and were used between 20 hpf and 48 hpf, unless otherwise stated. No statistical method was used to predetermine sample size for experimental groups.

Time-lapse imaging.

For confocal microscopy live embryos were mounted in 1% low melting agarose in glass bottom dishes, which were subsequently filled with media supplemented with 0.0045% 1-Phenyl-2-thiourea and 0.1% tricaine, as described previously[43,44]. Embryos were imaged using 20x or 40x-dipping objectives on a Zeiss LSM 700 confocal microscope. Embryos were maintained at 28°C whilst imaging using an in-line solution heater and heated stage, both controlled by a dual channel heater controller (Warner Instruments). Stacks were recorded at least every 0.3 h.

Movie image analysis.

Quantification of fluorescence intensity was performed in ImageJ. Quantification of cell volume and cell area were performed in Imaris or ImageJ, respectively. For cell volume analysis, the surface area of each daughter tip cell was 3D rendered in Imaris by manually tracing the mCherry-labelled membrane surface for each slice of multi-slice z-stack though cells of interest. The Imaris software then used to directly calculate the volume of 3D rendered cells. To calculate cell area, the shape of cells

was manually traced in ImageJ using 2D z-projections of cells of interest prior to quantification of the area of traced cells. Tracking of cells was also performed in ImageJ using the manual tracking plugin. All cell tracking recordings were normalised at each time point relative to the position of the dorsal aorta to account for any dorsal or ventral drift of embryos during imaging.

Morpholino and DNA construct injections.

To knock down *dll4* gene expression, embryos were injected at the one-cell stage with 5 ng control MO or 5 ng *dll4* MO. MO sequences were: 5'-CCTCTTACCTCAGTTACAATTTATA-3' (control)[44], 5'-GTTCGAGCTTACCGGCCACCCAAAG-3' (*dll4*)[5]. All MOs were purchased from Gene Tools. To generate mosaic lyn-mCherry-expressing endothelial cells, the 7 kb *kdrl* promoter[41] was used to transiently drive expression of lyn-mCherry using the Tol2 transposon system. Similarly, the *fli1* promoter and the Tol2 transposon system were used to drive transient mosaic expression of both lyn-mCherry and α-tubulin-GFP[45]. One-cell stage embryos were injected with 50 pg plasmid and 50 pg Tol2 transposase RNA.

Pharmacological treatments.

Embryos were manually dechorionated and incubated with compounds from 22 hpf (unless otherwise stated). The following compounds were used in this study: DBZ (2 μM), latrunculin B (0.08 μg/ml), SU5416 (0.3 μM, 0.6 μM or 2 μM), DMH4 (5 μM), Ki8751 (1 μM) and ZM323881 (80 nM, 160 nM or 5 μM).

Computational modelling.

For computational modelling we utilised the memAgent-Spring Model (MSM) of Vegf-Notch-mediated tip/stalk selection, as it has been well-validated against *in vivo* mouse and zebrafish ISV data in previous studies[20,21]. In this model, the endothelial

cell outer membrane is represented at a subcellular level by a collection of individual computational agents ("memAgents") connected by springs following Hooke's law, which represents the actin cortex beneath (see Supplementary Fig. 4a). The MSM allows subcellular level rules to generate localised responses of individual memAgents on the cell surface and complex cell shape changes during cell migration. In this study a new extension to the MSM model was developed and calibrated to the dimensions/parameters of *in vivo* data from Fig. 1a-e, (described below).

Initialisation: Three adhered endothelial cells were initialised at the bottom of a space between two "somites" calibrated to *in vivo* dimensions in Fig. 1a. Somites were modelled simply as space without Vegf signal to prohibit extension into them, similar to the approach used in ISV modelling with the MSM previously[21]. The two uppermost cells were designated the tip and stalk by a 25 h "warmup" period of Notch/Vegf signalling and filopodia dynamics before migration began, which establishes the spatiotemporal cellular patterning that would have occurred earlier in development. After this period, cell migration was then permitted to proceed by simulating the membrane forces involved in veil advancement, see below for details. Cells migrate to form the ISV with a calibrated probability of extending a filopodium either along the vertical Vegf gradient or in the furthest reachable direction. Vegf was calibrated to 0.9 + 0.0125 * y for each lattice site, after a wide parameter search, matching cell migration speeds against *in vivo* data (See Supplementary Fig. 3).

Migration: The MSM simulates veil advance along filopodium initiated by the agent at the tip of a filopodium, who propagates a signal down to the base, triggering release of adhesions along the filopodium that allows the membrane to advance. The spacing of filopodia was set at 2 microns, as previously measured[46]. The veil advance mechanism was modelled as a stochastic process, similar to its previous used to

model zebrafish ISVs[21]. We extended the realism of this mechanism to include an active lamella extension function, as well as a passive veil advance component. To do this the probability of veil advance was linked to the local Vegfr receptor activation. We call this Lamellar (*L*) extension of a memAgent (*m*), where L was treated as a stochastic function of its Vegfr (*V'*) activation (given as a proportion of the cells total Vegfrs (M_{tot}/V_{max})). Thus $P(L_m) = kV'_m M_{tot}/V_{max}$, where *k*(=*0.15*) is a constant, which was calibrated to match *in vivo* migration speeds (See Supplementary Fig. 3 and parameterization methods).

Division: to simulate cell division, firstly Three cells were initialised and exposed to a 25 h "warmup" period, as for simulations of non-dividing cells. Then, 1) a partitioning mechanism for intracellular components was applied to the dividing cell in an instantaneous manner and 2) the cell and its direct neighbour were designated the daughter cells by simply overwriting the previous cell identities and states (Supplementary Fig. 4b). This allowed for a focused exploration of the cell's ability to differentially partition cellular components between daughter cells of equal size, without introducing too many new variables.

Genetic-regulation extension: we adapted the gene-regulatory network (GRN) employed by the MSM in order to simulate partitioning during division. The original MSM model utilises a coarse queue representation of signal transduction and protein synthesis to abstract the passage of time and space between the activation of receptors at the membrane, gene expression changes in the nucleus and subsequent protein synthesis/trafficking of new receptor levels back to the cell surface[47]. The extension here delineates between each stage explicitly in the computational queue to clearly separate Notch receptor signal transduction/trafficking (DT), nuclear transcription and subsequent translation (DN) and Vegfr synthesis/trafficking (DS; Supplementary Fig.

4a). The same queue lengths as those in the standard MSM model were used, including queue DS that corresponds to the half-life of Vegfr, which tends to be reported in the range of 1-2 h[22-24] (see methods for details on the GRN queues).

Partitioning of Vegfr protein: Vegfr partitioning was simulated by dividing the mother cell's existing, synthesised Vegfrs between the daughters (held in the synthesis delay (DS) region of the queue representing post-nuclear activity). The half-life of Vegfr protein was set in the range of 1-2h, as previously reported[22-24]. A simple partition ratio to simulate symmetric (50:50 ratio) to severe asymmetric (100:1 ratio) division was used. In the symmetric case this yields daughter cells with initially less protein than mature cells, consistent with daughters initially having less cytosol than mature cell, but protein levels quickly recover to those of mature cells.

Partitioning of vegfr mRNA: In order to simulate asymmetric Vegfr receptor synthesis the MSM parameter $Vegfr_{tot}$, which represents the cells current total level of Vegfrs at the membrane, with synthesis and degradation balanced, was scaled by a recovery parameter *r*. The corresponding equation of Vegfr synthesis was thus $Vegfr_{tot} = r(V_{max} - N''_c\sigma)$, where V_{max} is the maximum Vegfr level, for $r = 1$, N''_c is the level of Notch intracellular domain (NICD) effective in the nucleus and σ is the strength of Vegfr down regulation due to activated Notch1. For asymmetric simulations, mRNA was enhanced in the leading dorsal daughter cell (cell 1.1), and reduced in the ventral daughter cell (cell 1.2). The best matching recovery of normal synthesis was set as follows:

$$r = \left(2 - \frac{(t_{recovery} - t_{timer})}{t_{recovery}}\right),$$

for the dorsal daughter cell and

$$r = \frac{(t_{recovery} - t_{timer})}{t_{recovery}},$$

for the ventral daughter cell, where t_{timer} is a timer that counts down incrementally starting at division time (initially $t_{timer} = t_{recovery}$), and $t_{recovery}$ is the time until normal mRNA levels recover (see Supplementary Table 1 for value, and parameterization section for calibration details). When evaluating symmetric receptor synthesis the GRN operates using the standard MSM model.

Cell Membrane asymmetry: Cell membrane asymmetries were achieved by initializing daughter cells with asymmetric numbers of memAgents. This is accomplished by allocating rows of memAgents according to the predefined ratios. In these studies we initialize the membrane asymmetry post-division to a maximum of 3:1, with the dorsal daughter 3 times the size of the ventral daughter.

Cell growth: to ensure growth of daughter cells back to normal size, a mechanism for membrane growth was introduced to the MSM. Membrane growth is achieved by recruiting new memAgents to the most extended spring in a cell's membrane. The mechanism governing recruitment in this case is linked to the rate at which daughter cells recover to a symmetric state. The smaller daughter cell grows at a rate of $\frac{(t_{recovery} - t_{timer})}{t_{recovery}}$, both parameters are the same as those used for mRNA.

Partitioning of actin: The MSM model incorporates an abstraction of actin dynamics in order to simulate the cytoskeletal dynamics underlying filopodia and lamellipodia extension/retraction. This abstraction represents the pool of available actin using a token system to allocate monomers to particular recruitment sites stochastically driven by local Vegfr activity. More details on the simulation of cytoskeleton are available in[47]. Simulation of asymmetric actin partitioning was achieved by adjusting the actin available to each cell to a particular asymmetry. The specific form of the asymmetry is the same as the recovery rate presented above for mRNA: $r = (2 -$

$\frac{(t_{recovery}-t_{timer})}{t_{recovery}}$) for the dorsal daughter cell and $r = \frac{(t_{recovery}-t_{timer})}{t_{recovery}}$, for the ventral daughter cell, both parameters are the same as those used for mRNA. The behavior under this mechanism was very similar to alternative asymmetric mechanisms, and was favored both because of the biological plausibility of such a recovery rate and parsimony in matching the mRNA mechanism. Under normal conditions with symmetric actin, both cells would have equal amounts of available actin according to the standard MSM model.

Dll4 kockdown conditions: *dll4* knockdown was simulated by setting endothelial cell Dll4 levels to zero for the entire duration of simulation. Otherwise, conditions with normal Dll4 expression were called "control."

Parameterisation of the computational model.

The simulation was first calibrated to match the *in vivo* control and *dll4* knockdown cases in the absence of cell division by adjusting the probability of extending a filopodium along the Vegf gradient [p_d], the probability of lamella advance [k], and the slope of the Vegf gradient across a range of values, as well as the Vegf environment to the set of parameters that can generate matching motility (Supplementary Fig. 3a). Parameters were chosen based upon the time it takes to fully extend the ISV, and the difference in rates between the two ventral cells. In the case of p_d and k values greater than the maximums (shown in Supplementary Figure 3a), they were saturated with respect to the observed behavior, for these cases the lowest values that generated the matching behavior were used. All parameter values are listed in Supplementary Table 1.

Cell size difference: In evaluating membrane size asymmetry, an extreme case of 3:1 was first chosen. Due to the discrete representation of the membrane, a larger ratio

yields a dorsal daughter with an insufficient number of memAgents to function reasonably.

Parameterization of recovery rates: We used an estimated rate of recovery of 8.3 h for normal Vegfr production, which aligns closely with the experimentally observed half-life of *VEGFR-2* mRNA[22,23]. Using an argument of parsimony, the same recovery rate was then used to govern the recovery rates of alternative mechanisms, such as actin and cell size.

Fluorescent in situ hybridisation (FISH).

Riboprobes were synthesised from *kdrl* and *egfp* PCR templates with T7 RNA polymerase. Primers used for generating PCR template-derived riboprobes were: 5'-CAAAATGACTCCTCTTAAAACCTCA -3' (*kdrl* forward), 5'-**AATACGACTCACTATAGGG**GATTCTCATGGTCCGGTTGC-3' (T7 *kdrl* reverse), 5'- GGAAGGATCCGCCACCATGGTGAGCAAGGGC-3' (*egfp* forward), 5'- **AATACGACTCACTATAGGG**TTACTTGTACAGCTCGTCCATG -3' (T7 *egfp* reverse). T7 promoter sequence is shown in bold. For double fluorescent *in situ* hybridisation, *Tg(kdrl:nlsEGFP)*^{zf109} embryos were imaged for the indicated periods, fixed in ice cold 4% paraformaldehyde then incubated at 4°C overnight. Embryos were then dehydrated in methanol for at least 2 h at -20°C. After rehydration, embryos were treated with 10 µg/ml proteinase K for 20 min and re-fixed with 4% paraformaldehyde. Embryos were incubated in hyb+ solution (50% formamide, 5x SSC, 9,2 µM citric acid, 500 µg/ml tRNA, 50 µg/ml heparin and 0.1% Tween-20) for 5 h at 60°C and then in fresh hyb+ solution containing 0.3 µg/ml *kdrl* and *egfp* antisense riboprobes labelled with digoxigenin (DIG) and dinitrophenol (DNP), respectively, and incubated overnight at 60°C. After hybridisation, embryos were washed in hyb- solution (50% formamide, 5x SSC, 9,2 µM citric acid and 0.1%

Tween-20) at 60°C and then in mixtures containing decreasing concentrations of hyb- and increasing concentrations of 2x SSC. Subsequently, embryos were washed in 0.2x SSC, then gradually washed into PBS with 0.1% Tween-20 (PBT) and finally into 1x maleic acid buffer (MAB). To detect the DIG-labelled riboprobe, embryos were incubated in blocking solution (1x MAB, 2% blocking reagent (Roche) and 20% lamb serum) for 1 h and then in fresh blocking solution containing 0.15 U/ml horse-radish peroxidase (POD) conjugated anti-DIG antibody (Roche; 11207733910) overnight at 4°C. After washing with 1x MAB, embryos were incubated in 1X plus amplification diluent (PerkinElmer) for 10 min, subsequently treated with Cyanine-3 Tyramide solution (1:100 in fresh diluent, PerkinElmer) for 30 min and washed in PBT overnight at 4°C. To detect the DNP-labelled riboprobe, embryos were incubated in blocking solution for 1 h and then in fresh blocking solution containing 1:500 POD conjugated anti-DNP antibody (PerkinElmer; FP1129) overnight at 4°C. Embryos were then washed with 1x MAB, incubated in 1X plus amplification diluent for 10 min, treated with Cyanine-5 Tyramide solution (1:100 in fresh diluent, PerkinElmer) for 30 min and finally washed in PBT overnight at 4°C.

Immunostaining following FISH

FISH-stained embryos were washed twice for 1 h at room temperature in 1x BBT (PBS, 1% BSA, 0.1% Triton X-100) prior to blocking for 1 h in BBT containing 2% HTLS. Primary antibody (Mouse anti-ZO-1-1A12, ThermoFisher Scientific, 1:200)[39] was incubated with embryos in block solution overnight at 4°C. Embryos were then washed four times for 1 h at room temperature in 1x BBT prior to incubation with block solution for 1 h and incubation with secondary antibody overnight at 4°C (AlexaFluor 405 anti-mouse; ThermoFisher Scientific; A-31553; 1:500). Finally, embryos were washed for once for 1 h at room temperature in 1x BBT, three times for

1 h at room temperature in 1x PBT (PBS, 0.1% Tween 20) and overnight at 4°C in PBT prior to imaging.

pErk Immunostaining.

Tg(kdrl:nlsEGFP)^{zf109} embryos were monitored by live-imaging up to the indicated time points either prior to or beyond the initiation of mitosis, and then rapidly fixed upon immersion in ice-cold 4% PFA overnight. Immunohistochemistry was then performed as previously[48] with a few changes. Briefly, fixed embryos were washed in 100% MeOH prior to incubation with 3% H_20_2 in MeOH on ice for 60 min and further 100% MeOH washes. Embryos were stored at -20°C for 2 days in MeOH. Embryos were then equilibrated with PBT (PBS, 0.1% Tween-20) washes and then cryoprotected in 30% sucrose in PBT overnight at 4°C. The next day embryos were equilibrated in PBT, incubated with 150 mM Tris-HCl (pH 9.0) for 5 min and then heated to 70°C for 15 min. Embryos were then washed with PBT and then twice with dH_2O for 5 min. Water was then removed prior to addition of ice-cold acetone for 20 min at -20°C. Acetone was removed prior to PBT washes, one TBST (TBS, 0.1% Tween-20, 0.1% Triton X-100) wash and incubation overnight at 4°C with block solution (TBST, 1% BSA, 10% goat serum). The next day embryos were then incubated with anti-phospho-ERK1/2 antibody (1:250, Cell Signalling; #4370) in blocking buffer overnight at 4°C. Washes in TBST at room temperature were followed by a wash in Maleic buffer (150 mM Maleic acid, 100 mM NaCl, 0.001% Tween-20, pH 7.4) for 30 min. Embryos were then blocked in 2% blocking reagent (Roche) in Maleic buffer for 3 h at room temperature prior to incubation with goat anti-rabbit IgG-HRP (1:1000) in 2% blocking reagent in Maleic buffer overnight at 4°C. Embryos were then washed in Maleic buffer and then PBS at room temperature prior to incubation with 50 µl amplification diluent with 1 µl Tyramide-Cy3 (Perkin

Elmer) for 3 h at room temperature in the dark. Embryos were finally washed over several days in TBST at room temperature. Levels of pErk were quantified as the mean nuclear Cy3 fluorescence intensity using ImageJ.

Statistics and Reproducibity

All statistical analyses were performed using GraphPad Prism 6.0 or Microsoft Excel software. Results are presented as mean ± S.E.M. All experiments were repeated at least three times and exact *n* is stated in the corresponding figure legend. Statistical significances of cell numbers, fluorescence intensity, size, or filopodia numbers were assessed using unpaired two-tailed Student's *t*-test. Statistical significances of cell motilities were assessed using two-way ANOVA test. Correlation of data sets was assessed using Pearson Correlation. For all analyses $P < 0.05$ was considered statistically significant. Statistical methods were not used to predetermine sample size, which varies with each experiment. Experiments were not randomized. The investigators were not blinded to allocation during experiments and outcome assessment. No samples were excluded from the analyses.

Code availability

The MSM model has been previously published[20,21]. New code to facilitate cell division and lamella extension/retraction functionality are available upon request

Data availability

All data supporting the findings of this study are available from the corresponding author upon reasonable request.

Supplementary Figure 1: TC and SC behaviour during ISV sprouting. (**a**) Predicted outcome of TC division and competitive Dll4-Notch-mediated re-selection of daughter tip/stalk identity. (**b**) Time-lapse images of sprouting ISVs from 22 hours post-fertilisation (hpf) in *Tg(kdrl:nlsEGFP)*^{zf109} embryos. (**c**) Quantification of the dorsal movement of individual tracked nuclei (*n*=7 ISVs, 2 embryos). (**d**) Quantification of the dorsal movement of tracked cells from **Fig. 1e** with error bars represented mean ± S.D. to show the intrinsic data variance (*n*=136 ISVs, 34 embryos). (**e**) Percentage of ISVs that contain TCs and/or SCs that did or did not divide following live-cell imaging from 22 to 32.5 hpf. Non-dividing TCs and SCs are labelled 1 and 2 respectively. Daughters of TC and SC divisions are labelled 1.1 / 1.2 and 2.1 / 2.2, respectively. 76% of TCs (14% + 40% + 22%) and 27% of SCs (22% + 5%) divided during ISV sprouting. (**f**) Time-lapse images of TCs that divided before or after nuclei had reached the horizontal myoseptum (HM; red dashed line). Brackets indicate dividing TCs. nlsEGFP spreads throughout the cell body upon initiation of division at 0.3 h, then daughter nuclei are pulled to the dorsal and ventral poles by 0.6 h later. Consequently, all analysis of post-mitotic cell behaviour was recorded at least 0.6 h after initiation of division and completion of cytokinesis. Moreover, cells that divide past the HM frequently had already reached the DLAV position resulting in distal daughters being pulled to the dorsal pole / DLAV position during division. Hence, the post-mitotic behaviours of daughters from divisions occurring past the HM were disregarded. (**g** and **h**) Quantification of the dorsal movement of daughters from tip (**g**) or stalk (**h**) cell divisions from **Fig. 1i** with error bars represented as mean ± S.D. to show the intrinsic data variance (*n*=43 ISVs, 1.1/1.2; *n*=41 ISVs, 2.1/2.2, 34 embryos). Nuclei are pseudocoloured according to their initial position. Error bars: mean ± SEM unless otherwise stated. **P*<0.0001 cell 1.2 in **g** versus cell 1 in **d**.

P<0.0001 cell 2.2 in **h versus cell 2 in **d**. two way ANOVA test. Scale bars, 25 μm.

Supplementary Figure 2: TC and SC behaviour upon disruption of Notch signalling. (**a**) Quantification of the total number of cells per ISV at 32.5 hpf, number of mitotic TCs or SCs per ISV, position of TC or SC divisions and the time of TC or SC divisions in control or DBZ-treated *Tg(kdrl:nlsEGFP)*^{zf109} embryos following live-cell imaging from 22 to 32.5 hpf (n=72 ISVs, 20 embryos, control; n=97 ISVs, 24 embryos, DBZ). More endothelial cells sprout into ISVs and more SC divisions are observed upon inhibition of Notch. (**b**) Quantification of the dorsal movement of daughter endothelial cells following TC and SC division upon incubation of embryos with DBZ (n=40 ISVs, 26 embryos). Dashed lines represent endothelial cells motilities from **Fig. 1e**. (**c**) Time-lapse images of daughter cells in *Tg(kdrl:nlsEGFP)*^{zf109} embryos following simultaneous division of both a tip and stalk cell and (**d**) quantification of the dorsal movement of daughter cells from tip and stalk cell divisions that occur within 4 h from each other (n=11 ISVs, 9 embryos). The distal daughter of stalk cell divisions are more motile than the proximal daughters of tip cell divisions despite residing more proximal in the ISV sprout. Error bars: mean ± SEM. *P<0.05 DBZ versus control. Unpaired two-tailed Student's t test. Scale bars, 25 μm.

Supplementary Figure 3: Computational modelling of endothelial cell migration. (**a**) Endothelial cell migration was modelled using an extended MemAgent-Spring Model (MSM; see Methods and **Supplementary Fig. 4a**), which introduces enhanced Vegf-stimulated lamellar extension. This model was calibrated to first match

experimental observations of ISV growth in the absence of cell division in control and *dll4* knockdown embryos (from **Fig. 1e** and **Fig. 2b**). Vegf gradient slope, concentration and biomechanical migration parameters were co-varied to find combinations that matched migration *in vivo* (Red boxes in **a**). (**b** and **c**) Quantitative simulation of migrating endothelial cells in the absence of division in either control (**b**) or *dll4* knockdown (**c**) conditions using the optimized parameters from **a** (n=10). Environmental Vegf gradient increases dorsally (green). In control simulations and upon *dll4* knockdown, *in silico* migration dynamics closely match those observed *in vivo*. Error bars: mean ± SEM.

Supplementary Figure 4: Computational modelling of cell division. (**a**) Schematic of the MSM internal signalling. The total number of activated Notch receptors is added to the top of a queue and moves through one place each time step (t) to simulate the time it takes to affect gene regulation and protein synthesis. Queue height = time delay D1 = Σ trafficking (DT), transcription (DN) and synthesis times (DS). Notch activity after D1 reduces Vegfr expression. (**b**) Initialisation configuration of the MSM for TC division simulations. After an initial warm-up period to establish tip and stalk identities prior to division (initialisation step), MSM queues were partitioned between two daughter cells from a tip cell division by overwriting cell states (division step) prior to a period of growth to monitor post-mitotic cell motilities (migration step). Environmental VEGF gradient increases dorsally (green). (**c** to **h**; n=10) Quantification of post-mitotic cell motility following simulation of TC divisions in either control (**c**, **e**, **g**) or *dll4* knockdown (**d**, **f**, **h**) conditions upon asymmetric partitioning of either cell membrane surface area (**c**, **d**; extreme 3:1 distal/proximal ratio), Vegfr protein (**e**, **f**; extreme 100:1 distal/proximal ratio) or

vegfr mRNA (**g**, **h**; double the production of Vegfr protein in distal versus proximal cells). (**c**, **d**) Extreme asymmetry of cell surface area alone was insufficient to replicate *in vivo* data. (**e**, **f**) Moreover, even upon extreme Vegfr protein asymmetry, the duration of the asymmetric migration of daughter cells does not recapitulate biological observations due to rapid recovery of the protein pool by symmetrically partitioned *vegfr* mRNA. (**g**, **h**) In contrast, more prolonged asymmetry was observed upon differential Vegfr protein synthesis due to *vegfr* mRNA asymmetry, generating post-mitotic behaviours that predominantly matched control and *dll4* knockdown conditions. Error bars: mean ± SEM.

Supplementary Figure 5: TC divisions are asymmetric during ISV and MsV branching. (**a**) Time-lapse images of rEos fluorescence in a dividing photo-converted ISV tip cell and quantification of rEos levels in single confocal slices through the centre of dividing cells at the indicated time points (*n*=6 dividing cells). Arrowheads in **a** indicate the position of the cleavage furrow formed during cytokinesis. (**b**) Bright field and fluorescence images of the heads of 48 hpf *Tg(kdrl:GFP)*^{s843} embryos indicating the positions of the MsV and MCeV. (**c**) Time-lapse images of a branching MsV from 24 hpf. (**d** and **e**) Time-lapse images of gEos fluorescence and rEos heat maps in a dividing photo-converted MsV TC (**d**) and quantification of rEos levels inherited by each TC daughter, as well as the total rEos fluorescence present before (cell 1) and after (cells 1.1 + 1.2) TC division (**e**, *n*=5 dividing TCs from 5 embryos). Bracket indicates dividing cell. Error bars: mean ± SEM. *P<0.001 1.1 versus 1.2. Unpaired two-tailed Student's t test. Scale bars, 25 μm.

Supplementary Figure 6: Asymmetric division is not driven by differential partitioning of filopodia. (**a**) Time-lapse images of a dividing lyn-mCherry-expressing TC and quantification of total filopodia both before (cell 1) and directly after (cell 1.1 and cell 1.2) TC division (*n*=8 dividing TCs from 6 embryos). In all images, brackets and arrowheads indicate mitotic TCs and the *de novo* interface between daughter cells, respectively. Distal daughters of TC division inherit significantly more filopodial protrusions. (**b**) Correlation of the total number of filopodia possessed by individual TC daughters with their rate of post-mitotic motility (P<0.01. Pearson's correlation. R2=0.63. *n*=12 cells from 5 embryos). (**c**) lyn-mCherry-expressing TCs in control or latrunculin B (lat. B)-treated *Tg(kdrl:nlsEGFP)*^{zf109} embryos at 24 hpf, and quantification of total TC filopodia (*n*=8 TCs, 8 embryos, control; 7 TCs, 7 embryos, lat. B). (**d** and **e**) Time-lapse images of non-dividing (**d**) or dividing (**e**) individual lyn-mCherry expressing TCs in lat. B-treated embryos from 22 hpf. Bracket in **e** indicates a mitotic TC. (**f**) Quantification of dorsal movement of the cell nuclei and top, bottom and centre of the migrating TC in panel **d** (*n*=1). (**g**) Quantification of the averaged motility of tracked endothelial cell nuclei both in the absence of division (cells 1 and 2 from 22 hpf; *n*=63 cells for 1 and *n*=46 cells for 2, from 9 embryos) and after TC division (cells 1.1 and 1.2; *n*=28 cells from 9 embryos). In the absence of filopodia, TC divisions still generate asymmetric daughters. (**h**) A dividing lyn-mCherry-expressing TC in a lat. B-treated embryo and quantification of cell size both before (cell 1) and directly after (cell 1.1 and cell 1.2) TC division (*n*=7 dividing TCs from 7 embryos). (**i**) Quantification of the dorsal movement of TC daughters of the indicated sizes in lat.B-treated embryos (*n*=10 cells from 5 embryos). (**j**) Correlation of the size of individual TC daughters with their rate of post-mitotic motility in lat. B-treated embryos (P<0.01. Pearson's correlation.

R2=0.70. *n*=10 cells from 5 embryos). In the absence of filopodia, TC daughter motility is still dependent on cell size. (**k**) *egfp* (green) or *kdrl* (red) mRNA localisation in ISVs of *Tg(kdrl:nlsEGFP)*^{zf109} embryos at 24 hpf. Arrows indicate distal accumulation of *kdrl* mRNA relative to *egfp*. (**l**) Time-lapse images of an nlsEGFP-expressing sprouting ISV and localisation of *egfp* (green) and/or *kdrl* (red) mRNA. Arrows indicate distal accumulation of *kdrl* mRNA at the leading edge of migrating endothelial cells. (**m**) Quantification of the distal enrichment of *kdrl* mRNA in sprouting ISVs. The ratio of *kdrl* versus *egfp* mRNA was calculated every 5 µm from the distal-most side of ISVs (n=69 ISVs, 13 embryos). (**n**-**p**) *egfp* (green) and either *cdh5* (**n**), *flt4* (**o**) or *flt1* (**p**, red) mRNA localisation in ISVs of *Tg(kdrl:nlsEGFP)*^{zf109} embryos at 24 hpf. Note no noticeable distal accumulation of mRNA. Error bars: mean ± SEM. *P<0.01 1.1 versus 1.2. **P<0.001 versus control. ***P<0.05 versus egfp. Unpaired two-tailed Student's t test. Scale bars, 25 µm.

Supplementary Table 1. MSM model dimensions and parameters. The dimensions and parameters used in MSM are listed.

Supplementary Table 2. Statistics source data. Source data for cell motility analyses in Fig. 1 to 6.

Supplementary Video 1: Time-lapse confocal movie of non-dividing endothelial cells in a branching ISV of a *Tg(kdrl:nlsEGFP)*^{zf109} embryo (from Supplementary data Fig. 1b). Embryos were imaged from 22 hpf for 9.6 h (0.3 h per frame). The leading TC is more motile than adjacent trailing SCs.

Supplementary Video 2: Time-lapse confocal movie of an individual lyn-mCherry expressing TC in a sprouting ISVs of a *Tg(kdrl:nlsEGFP)*^{zf109} embryo (from Fig. 1a). Embryos were imaged from 22 hpf for 4.5 h (0.3 h per frame). The TC is highly motile and migrates rapidly.

Supplementary Video 3: Time-lapse confocal movie of an individual lyn-mCherry expressing SC in a sprouting ISVs of a *Tg(kdrl:nlsEGFP)*^{zf109} embryo (from Fig. 1b). Embryos were imaged from 22 hpf for 7.2 h (0.3 h per frame). The SC does not rapidly migrate and undergoes cell elongation.

Supplementary Video 4: Time-lapse confocal movie of a dividing TC in a branching ISV of a *Tg(kdrl:nlsEGFP)*^{zf109} embryo (from Fig. 1g). Embryos were imaged from 22 hpf for 7.2 h (0.08 h per frame). The distal daughter of TC division (cell 1.1) is more motile than the proximal daughter (cell 1.2).

Supplementary Video 5: Time-lapse confocal movie of a dividing SC in a branching ISV of a *Tg(kdrl:nlsEGFP)*^{zf109} embryo (from Fig. 1h). Embryos were imaged from 22 hpf for 7.2 h (0.08 h per frame). The distal daughter of SC division (cell 2.1) is slightly more motile than the proximal daughter (cell 2.2).

Supplementary Video 6: Time-lapse confocal movie of non-dividing endothelial cells in a branching ISV of a *dll4* knockdown *Tg(kdrl:nlsEGFP)*^{zf109} embryo (from Fig. 2a). Embryos were imaged from 22 hpf for 10.2 h (0.3 h per frame). In the absence of *dll4*, all cells display TC-like motilities and accumulate in DLAV position.

Supplementary Video 7: Time-lapse confocal movie of a dividing TC in a branching ISV of a *dll4* knockdown *Tg(kdrl:nlsEGFP)*^{zf109} embryo (from Fig. 2d). Embryos were imaged from 22 hpf for 10.2 h (0.3 h per frame). In the absence of *dll4*, the distal daughter of TC division (cell 1.1) is still more motile than the proximal daughter (cell 1.2) and a more motile adjacent SC (cell 2) overtakes the slower proximal daughter.

Supplementary Video 8: Time-lapse confocal movie of a dividing SC in a branching ISV of a *dll4* knockdown *Tg(kdrl:nlsEGFP)*^{zf109} embryo (from Fig. 2e). Embryos were imaged from 22 hpf for 10.2 h (0.3 h per frame). In the absence of *dll4*, the distal daughter of SC division (cell 2.1) is still more motile than the proximal daughter (cell 2.2) and is sufficiently hyper-motile to overtake an adjacent TC (cell 1).

Supplementary Video 9: Movies of MSM simulations of daughter cell behaviour following symmetric tip cell division. Tip cell daughter migration is disrupted by mutual repression of motile behaviour.

Supplementary Video 10: Movies of MSM simulations of daughter cell behaviour following asymmetric tip cell division. The distal daughter of tip cell division is highly motile relative to the proximal daughter.

Supplementary Video 11: Time-lapse confocal movie of an individual dividing TC expressing α-tubulin- GFP and lyn-mCherry in a *Tg(kdrl:ras-mCherry)*^{s896} embryo (from Fig. 4f)**.** Embryos were imaged from approximately 22 hpf for 25 min

(55 sec per frame). After initially assuming a central position, the entire mitotic spindle is shifted to the proximal pole during metaphase.

Supplementary Video 12: Time-lapse confocal movie of a dividing TC in a branching ISV of a 0.3 µM SU5416-treated *Tg(kdrl:nlsEGFP)*^{zf109} embryo (from Fig. 6c). Embryos were imaged from 22 hpf for 8.7 h (0.3 h per frame). In the presence of 0.3 µM SU5416, both daughters of TC division display similar SC-like motilities.

Supplementary Video 13: Time-lapse confocal movie of a dividing TC in a branching ISV of a *Tg(kdrl:nlsEGFP)*^{zf109} embryo (from Fig. 6g). Embryos were imaged from 22 hpf for 8.7 h (0.3 h per frame). The proximal daughter of TC division (cell 1.2) atypically overtakes the distal daughter (cell 1.1) and assumes the TC position.

Supplementary Video 14: Time-lapse confocal movie of a dividing TC in a branching ISV of a *Tg(kdrl:nlsEGFP)*^{zf109} embryo (from Fig. 6h). Embryos were imaged from 22 hpf for 8.7 h (0.3 h per frame). The proximal daughter of TC division (cell 1.2) is overtaken by the adjacent SC (cell 2).

Supplementary Figure 1

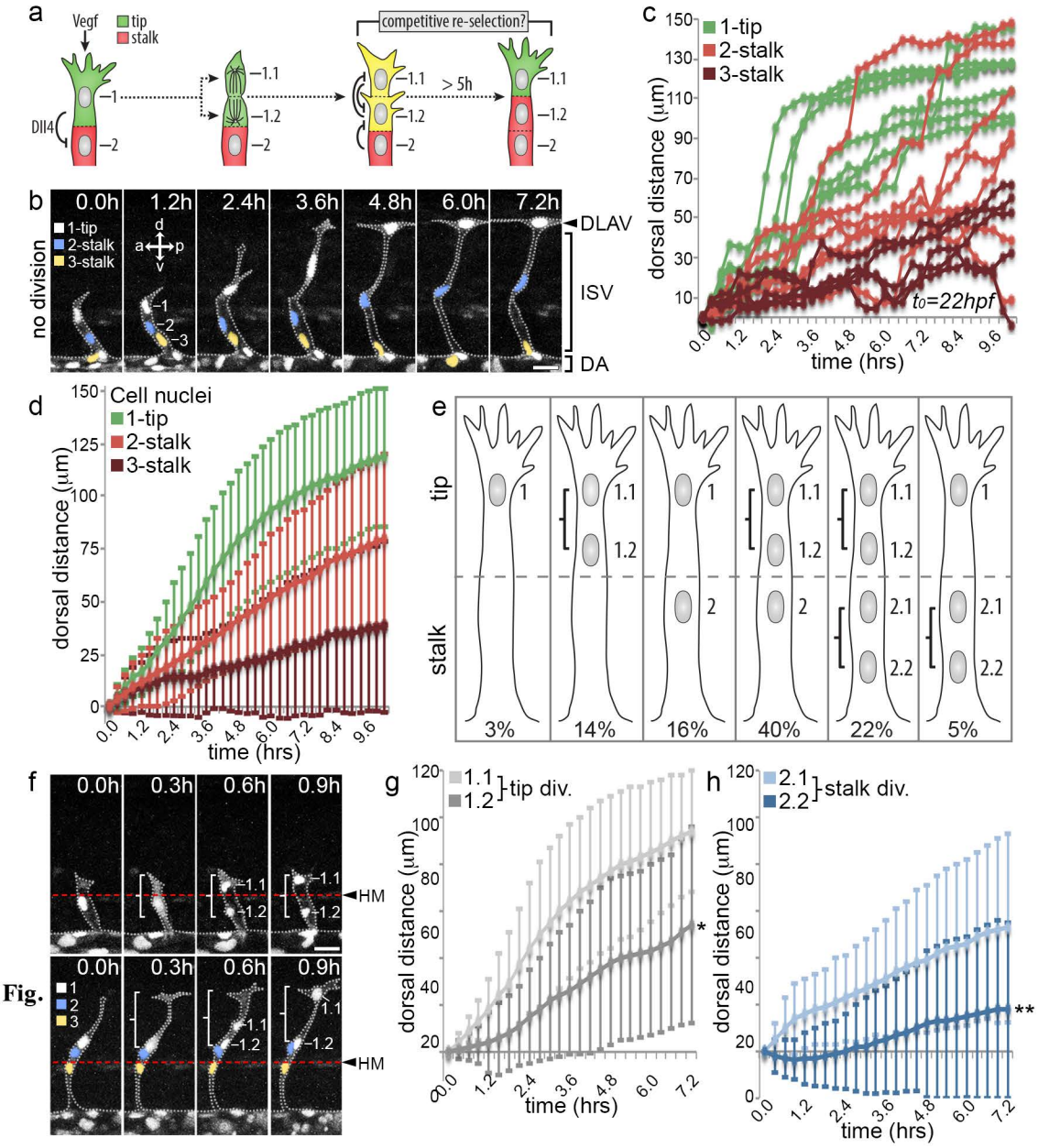

Supplementary Figure 2

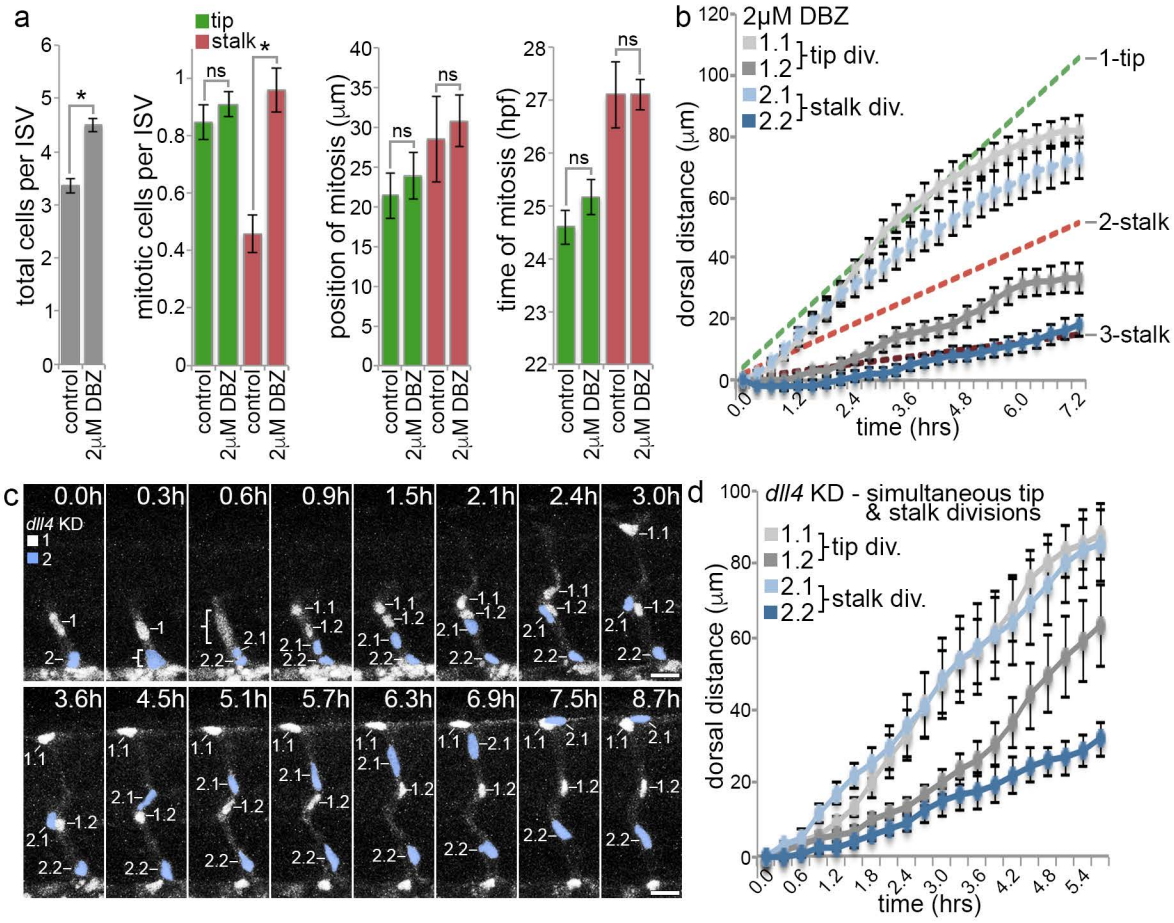

Supplementary Figure 3

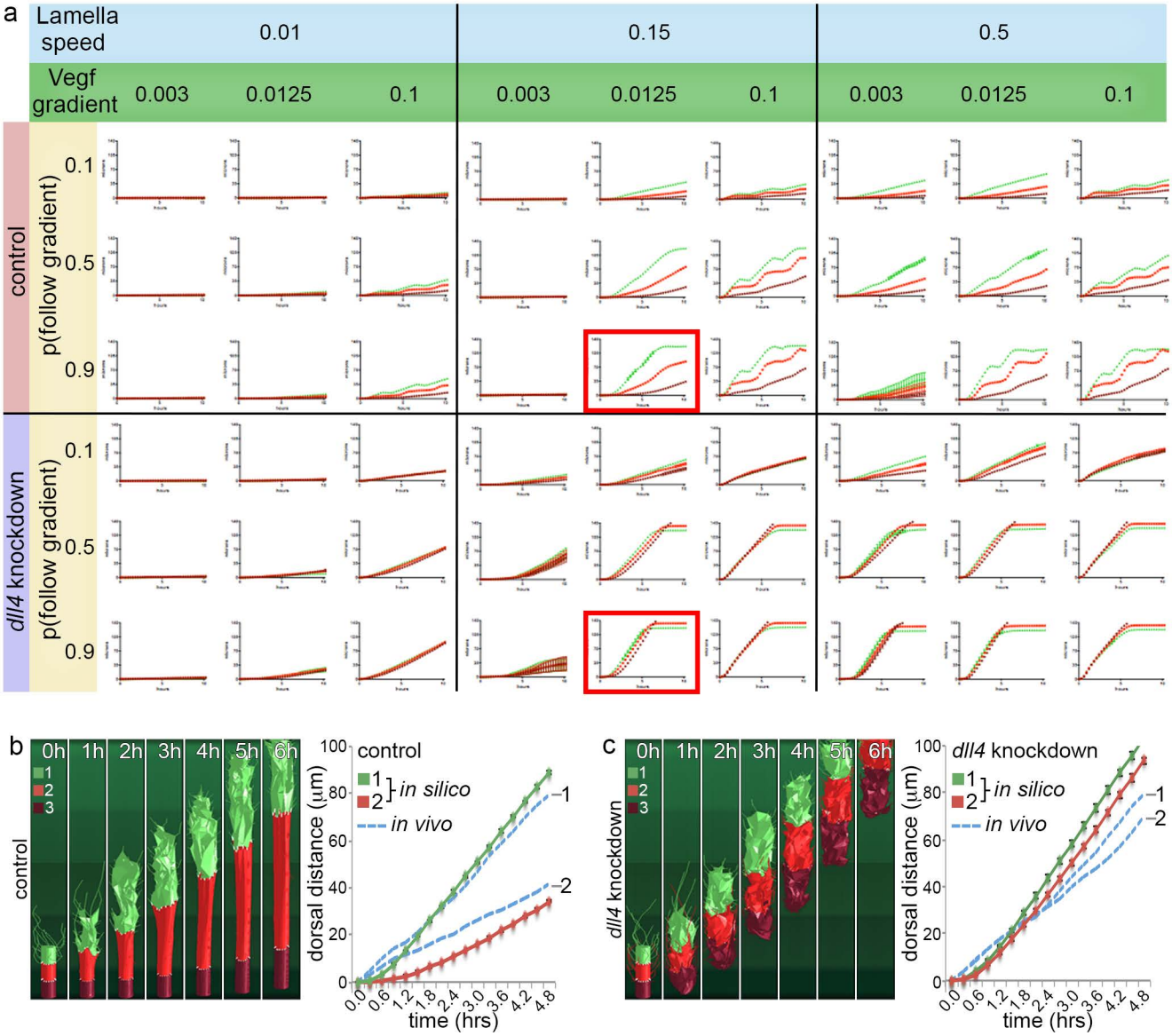

Supplementary Figure 4

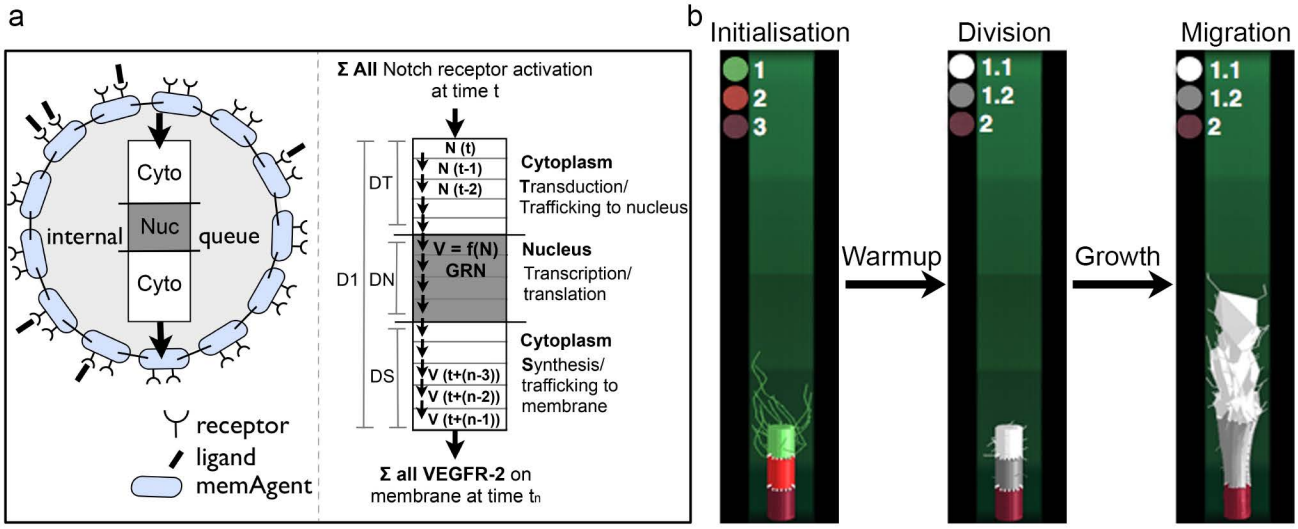

cell membrane surface area asymmetry

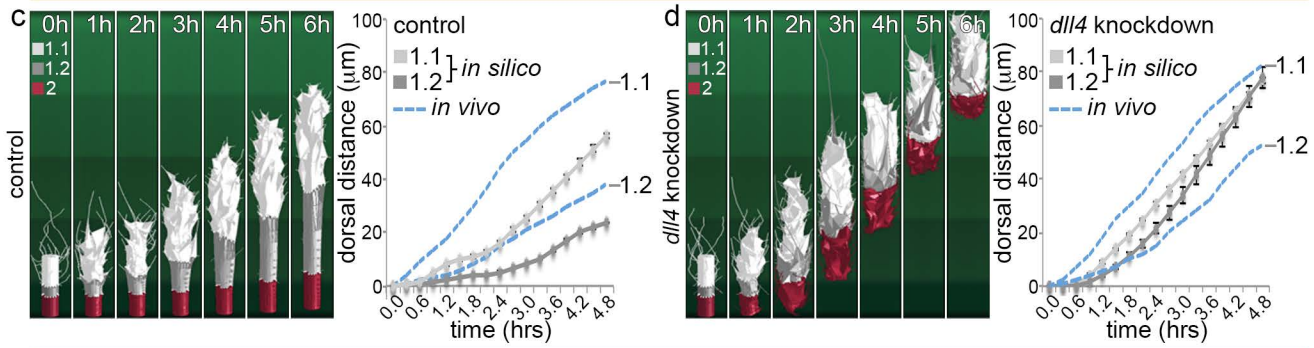

Vegfr protein asymmetry

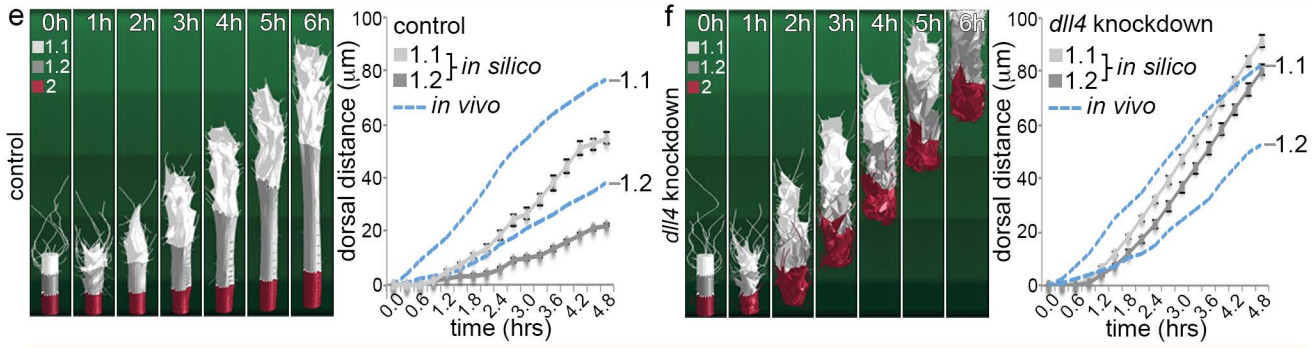

vegfr mRNA asymmetry

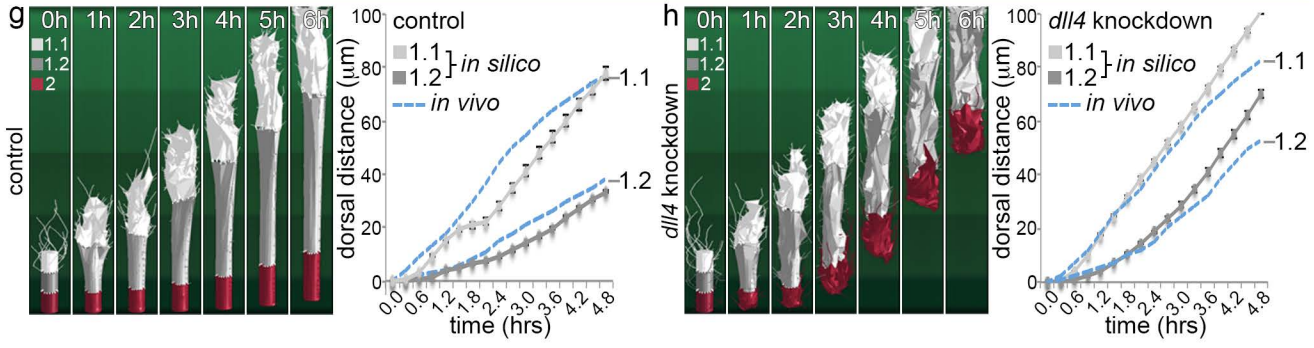

Supplementary Figure 5

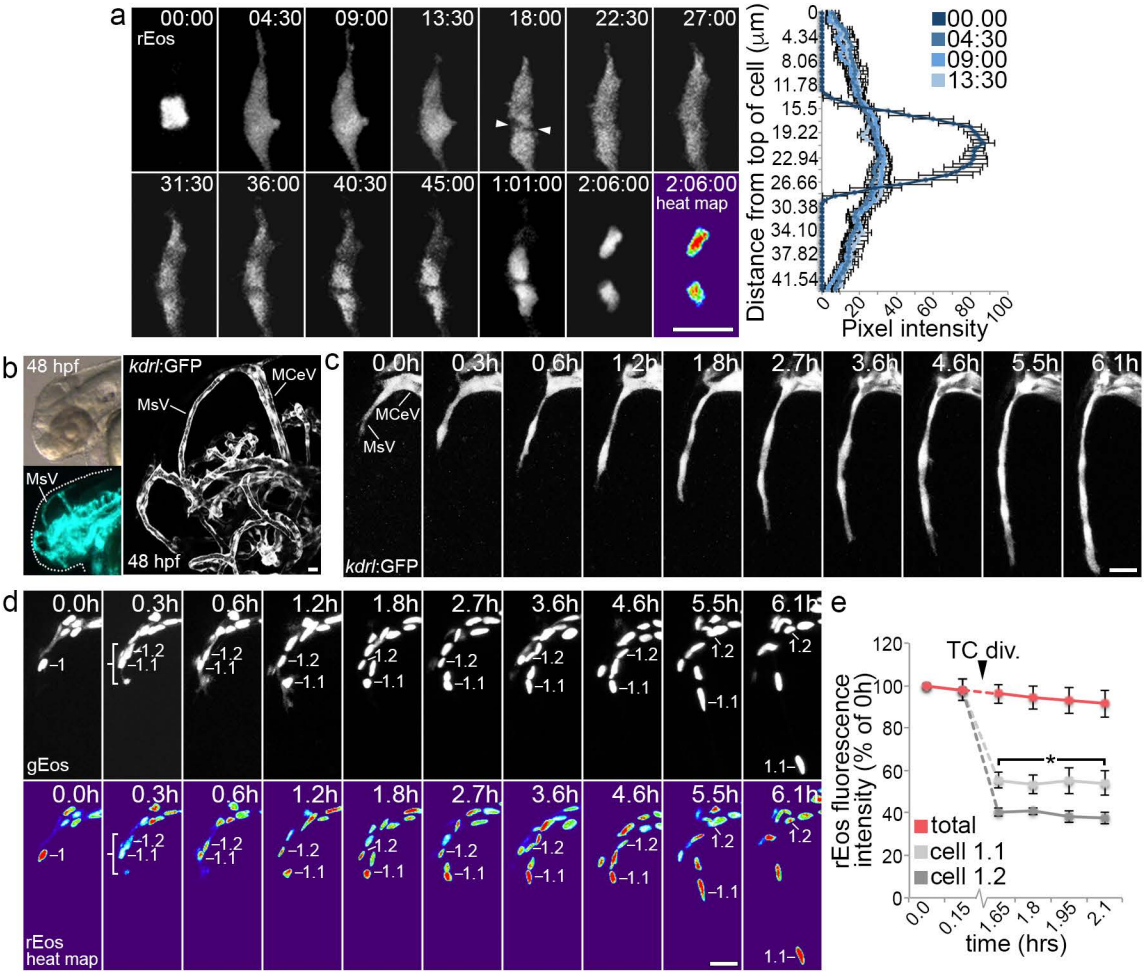

Supplementary Figure 6

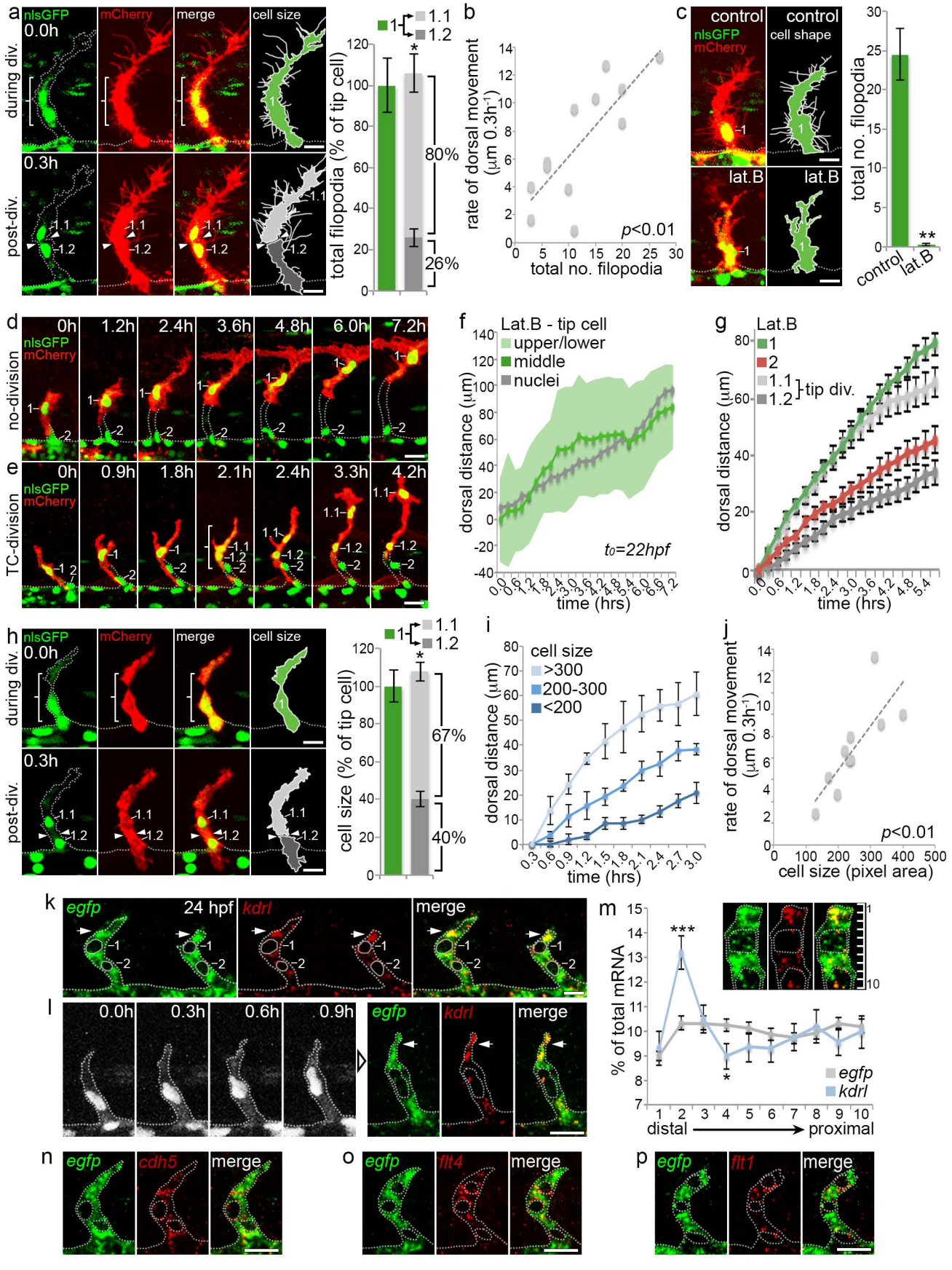

Supplementary Table 1. MSM model dimensions and parameters.

Parameter	Variable name	Value	Source
Filopodia spacing		2 microns	Measured previously[37]
Length of ISV	Xg	150 microns	Measured *in vivo* (e.g. Fig. 1)
Probability of filopodia in VEGF gardient/ dorsal direction	Pd	0.5 unitless	Calibrated to *in vivo* data (Extended Data Fig. 3a)
Rate of lamella advance	k	0.15 unitless	Calibrated to *in vivo* data (Extended Data Fig. 3a)
Warmup time	$t_{recovery}$	25 hrs	Model specific
Base VEGF level		0.9 molecules per grid site	Calibrated to *in vivo* data in the absence of divisions
VEGF slope		0.0125 along Y-axis	Calibrated to *in vivo* data (Extended Data Fig. 3a)
Recovery rate		8.3hrs	Calibrated to *in vivo* data (Extended Data Fig. 3a), within measured range[39,40]